AIChE

Finite Volume Method for Falling Liquid Films Carrying Monodisperse Spheres in Newtonian Regime

Patricio Bohorquez
Área de Mecánica de Fluidos, Departamento de Ingeniería Mecánica y Minera, Universidad de Jaén, Campus de las Lagunillas, 23071 Jaén, Spain

DOI 10.1002/aic.13863
Published online June 25, 2012 in Wiley Online Library (wileyonlinelibrary.com).

A finite volume method is proposed to study the dynamics of unsteady, falling liquid films carrying monodisperse spheres in Newtonian regime under the action of gravity. The Navier–Stokes equations were rewritten to implement a numerical scheme with interface capturing capability, able to compute discontinuities in the solid volumetric concentration and free surface flows. The interface capturing property is checked with simple benchmarks, showing that experimental data for a vertical settler and the dynamics of the wetting front in a thin liquid film are reproduced with success. Also, the numerical scheme computes with accuracy Kapitza instability or viscous roll waves. This work concludes illustrating the applicability of the model to study viscous resuspension phenomenon in a unsteady, falling suspension film. © 2012 American Institute of Chemical Engineers *AIChE J,* 58: 2601–2616, 2012
Keywords: thin film flow, particle migration, suspensions, viscous roll waves, two-layer film flow

Introduction

This study is aimed at modeling unsteady, falling liquid films carrying monodisperse spheres in Newtonian regime[1] under the action of gravity. A simple sketch of the problem on a constant slope bed is shown in Figure 1, where the existence of three phases is observed: liquid (*l*), solid (*p*), and gas (*g*). This work focuses on flows in which the solid and liquid phases define a suspension, provided that the solid phase remains within the liquid. Such situation is observed in many chemical processes of industrial interest in which the presence of monodisperse spheres introduces an additional difficulty with respect to the case of a thin-film flow of pure clear liquid due to variations of the solid volumetric concentration, see Usha et al.[2] and Kalliadasis et al.[3] for a comprehensive review.

Even in thin film flows, local inhomogeneities on the solid phase usually induce complex flow features that can be observed in a (larger) macroscopic scale, as described by Timberlake and Morris.[4] Consequently, it is important to take into account possible variations in the solid volumetric concentration both in the streamwise direction and along the perpendicular to the inclined plane in Figure 1. From the hierarchy of models described by Kalliadasis et al.,[3] see section 4.9.2 in their book,[3] the Navier–Stokes approach has been adopted here allowing to better understand the details of the flow dynamics. A similar approach was described by Min and Kim[5] for planar jet and slot coating flows in steady-state. Alternatively, reduced order models such as boundary-layer, averaged models, and single surface equations could be formulated, as well as more complex mesoscopic and microscopic models, see Fox.[6]

This work is hence motivated by a wish to propose a finite volume method able to compute unsteady falling liquid films carrying monodisperse spheres in Newtonian regime. The main new features are that the original set of partial differential equations governing the flow dynamics is rewritten in a way that it is easier to ensure good shock capturing properties of the numerical scheme extending Min and Kim's work.[5] Recall that unsteady free surface flow requires sophisticated numerical schemes to avoid difficulties associated with conservative differencing, spurious oscillations, and thickening of the interface, see for example Gopala and Van Wachem.[7] Furthermore, as it happens for gas-particle flow, numerical difficulties may develop when the solid phase concentration value is close to the maximum packing factor, see Passalacqua and Fox[8] and references therein. The formulation presented in this article complements previous models solving for the continuity and momentum balance equation of each phase, see van Wachem et al.,[9,10] because such equations are reformulated to yield a mixture model[11] for suspensions (i.e., solid–liquid mixture) flowing in an immiscible ambient fluid (i.e., gas phase). To the author's knowledge, results for unsteady falling liquid films carrying monodisperse spheres have not been reported beforehand by means of CFD solving for the full Navier–Stokes system of equations, which constitutes an outstanding problem. Indeed, this type of flow might be very complex also because of the development of free surface instabilities, see Ch. 1 in Kalliadasis et al.[3] Therefore, the capability of the algorithm to compute hydrodynamic instabilities must be checked as was done by Malamataris and Balakotaiah,[12] among others, for Kapitza instability or viscous roll waves.

The full mixture model is formulated for unsteady falling suspension films in Newtonian regime in the next section,

Correspondence concerning this article should be addressed to P. Bohorquez at patricio.bohorquez@ujaen.es.

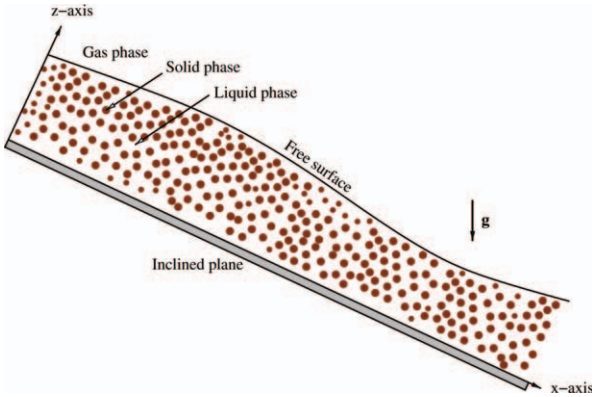

Figure 1. Sketch of a thin film flow carrying particles down an inclined plane.

[Color figure can be viewed in the online issue, which is available at wileyonlinelibrary.com.]

where it is shown that the formulation reduces to the classical volume of fluid (VOF) method[13] in the absence of solid particles. This model does not apply during the stopping phase of liquid-particle motion (when the maximum packing factor is being reached)—a rheological regime which is outside the scope of this work. Subsequently, a finite volume method is defined based on the Schur complement which is used to solve for the proposed formulation. The section entitled Results is devoted to present supporting numerical simulations that are validated with previous known results for vertical settlers, unsteady falling suspension films down an inclined plane and viscous roll waves in one- and two-layer thin film flows. A summary and some concluding comments are drawn in the section entitled conclusions.

Formulation of the Problem

Under the axiom of continuum,[14] the continuity equations of each phase are given by

$$\frac{\partial \alpha_l \rho_l}{\partial t} + \nabla \cdot (\alpha_l \rho_l \vec{v}_l) = 0 \tag{1}$$

$$\frac{\partial \alpha_p \rho_p}{\partial t} + \nabla \cdot (\alpha_p \rho_p \vec{v}_p) = 0 \tag{2}$$

$$\frac{\partial \alpha_g \rho_g}{\partial t} + \nabla \cdot (\alpha_g \rho_g \vec{v}_g) = 0 \tag{3}$$

In these equations, t is time, while ρ_k, α_k, and $\vec{v}_k$ represent the density, volumetric concentration, and conditionally averaged velocity of the kth phase, respectively ($k = l, p, g$). Because the solid phase cannot cross from the liquid to the gas phase, the phase volumetric concentrations $\alpha_{g,p}$ will be written as function of the volume fraction occupied by the solid–liquid mixture within a small control volume, say $\gamma \equiv 1 - \alpha_g$, and of the volumetric concentration of solid particles in the three-phase mixture, denoted by $\beta \equiv \alpha_p$. The axiom of continuity, that is, $\alpha_l + \alpha_p + \alpha_g = 1$, implies that the liquid volumetric concentration is given by $\alpha_l \equiv \gamma - \beta$.

The continuity equation of the mixture is readily deduced by adding Eqs. 1–3

$$\frac{\partial \rho}{\partial t} + \nabla \cdot (\rho \vec{v}) = 0 \tag{4}$$

in which ρ is the mixture density

$$\rho \equiv \rho_p \beta + \rho_l (\gamma - \beta) + \rho_g (1 - \gamma) \tag{5}$$

and $\vec{v}$ is mass-average velocity

$$\vec{v} \equiv \frac{1}{\rho}\left[\rho_p \beta \vec{v}_p + \rho_l (\gamma - \beta)\vec{v}_l + \rho_g (1 - \gamma)\vec{v}_g\right] \tag{6}$$

To simplify the notation, new variables characterizing the liquid-particle suspension were defined and denoted with the subscript m. The density (ρ_m), mass- ($\vec{v}_m$), and volume-average ($\vec{u}_m$) velocity in the liquid–solid suspension are given by the following expressions

$$\rho_m \equiv \rho_p \frac{\beta}{\gamma} + \rho_l \left(1 - \frac{\beta}{\gamma}\right) \tag{7}$$

$$\vec{v}_m \equiv \frac{1}{\rho_m}\left[\frac{\beta}{\gamma}\rho_p \vec{v}_p + \left(1 - \frac{\beta}{\gamma}\right)\rho_l \vec{v}_l\right] \tag{8}$$

$$\vec{u}_m \equiv \frac{\beta}{\gamma}\vec{v}_p + \left(1 - \frac{\beta}{\gamma}\right)\vec{v}_l \tag{9}$$

In addition, an alternative formulation of the mixture continuity equation (4) is required to formulate the pressure equation as the Schur complement because, as shown in the Finite Volume Discretisation and Solution Procedure, the role of the mixture pressure is the same as for single incompressible flows (i.e., to ensure continuity). Dividing the kth phase continuity equation (1)–(3) by the kth phase density and adding the resulting equations yields

$$\nabla \cdot \vec{u} = 0 \quad \text{with} \quad \vec{u} \equiv \gamma \vec{u}_m + (1 - \gamma)\vec{v}_g \tag{10}$$

This shows that the volumetric velocity $\vec{u}$ is a divergence-free vector.

Now the relative velocity of the solid particles with respect to the liquid is defined as

$$\vec{v}_r \equiv \vec{v}_p - \vec{v}_l \tag{11}$$

and the relative velocity of the dense suspension with respect to the gas phase is given by

$$\vec{u}_{r\gamma} \equiv \vec{u}_m - \vec{v}_g \tag{12}$$

Taking into account (8)–(12), it is an easy exercise to write $\vec{v}$ (6) in terms of $\vec{u}$ (10), $\vec{v}_r$ (11) and $\vec{u}_{r\gamma}$ (12) as

$$\vec{v} = \vec{u} + \gamma(1 - \gamma)\frac{\rho_m - \rho_g}{\rho}\vec{u}_{r\gamma} + \beta s \frac{\gamma - \beta}{\gamma + \beta s}\frac{\rho_m}{\rho}\vec{v}_r \quad \text{with} \quad s \equiv \frac{\rho_p}{\rho_l} - 1 \tag{13}$$

Interestingly, the effect of the relative velocity in the liquid-particle mixture is to cause a difference between the mass- and volume-average velocity. Thus, when slip velocities are not negligible, mass transfer is not necessarily accompanied by a similar volume transfer. The present formulation retains both velocities and, subsequently, requires to assess the difficulties in formulating a numerical scheme suitable for the model problem.

To formulate a conservative numerical scheme to solve for (1)–(3), it is convenient to rewrite these equations in terms of the divergence-free velocity field $\vec{u}$, instead of $\vec{v}_k$. Dividing (1) and (2) by ρ_l and ρ_p, respectively, and adding the ensuing equations, yields

$$\frac{\partial \gamma}{\partial t} + \nabla \cdot (\gamma \vec{u}) + \nabla \cdot [\gamma(1-\gamma)\vec{u}_{r\gamma}] = 0 \tag{14}$$

The equation for β requires some additional algebra. Eliminating $\vec{v}_l$ from (9) and (11), and $\vec{v}_g$ from (9) and (12), one can recast the velocity $\vec{v}_p$ as function of $\{\beta, \gamma, \vec{u}, \vec{u}_{r\gamma}, \vec{v}_r\}$

$$\vec{v}_p = \vec{u}_m + \left(1 - \frac{\beta}{\gamma}\right)\vec{v}_r = \vec{u} + (1-\gamma)\vec{u}_{r\gamma} + \left(1 - \frac{\beta}{\gamma}\right)\vec{v}_r \tag{15}$$

Now substituting (15) into (2), one finds

$$\frac{\partial \beta}{\partial t} + \nabla \cdot (\beta \vec{u}) + \nabla \cdot [\beta(1-\beta)\vec{u}_{r\beta}] = 0 \tag{16}$$

in which

$$\vec{u}_{r\beta} \equiv \frac{\gamma(1-\gamma)\vec{u}_{r\gamma} + (\gamma - \beta)\vec{v}_r}{\gamma(1-\beta)} \tag{17}$$

So the analogy between the scalar transport equation of the indicator function γ (14) and of the volumetric solid concentration β (16) becomes evident and, therefore, one can apply exactly the same numerical scheme to solve them. Notice that (14) and (16) reduce to the standard multi-dimensional advection equation for vanishing values of the relative velocities, being $\nabla \cdot \vec{u} = 0$ (10). Equations 14 and 16 constitute a system of hyperbolic balance laws, which may exhibit discontinuities in γ and β, and difficulties associated with conservative differencing. The main advantages of the present formulation is that it is easier to formulate fully conservative numerical schemes provided the incompressible constraint (10), see for example LeVeque.[15] In addition, if the gas phase is immiscible with respect to the solid–liquid suspension, that is, γ defines a thin interface, the free surface will remain sharp during the numerical simulation because the divergence operators in (14) vanish far from the interface (where γ takes the constant value of 0 or 1). Furthermore, in such scenario $\vec{u}_{r\beta} = 0$ and, subsequently, (14) equals the well-known VOF equation, see for instance Gopala and Van Wachem[7] and Unverdi and Tryggvason.[13]

Analogous, the axiom of continuum[14] allows to write the momentum balance equations of each phase, given by

$$\frac{\partial \alpha_l \rho_l \vec{v}_l}{\partial t} + \nabla \cdot (\alpha_l \rho_l \vec{v}_l \vec{v}_l) = \alpha_l \rho_l \vec{g} - (1-\alpha_p)\nabla p_l - K(\vec{v}_l - \vec{v}_p) + \nabla \cdot (\alpha_l \bar{\bar{\tau}}_l') \tag{18}$$

$$\frac{\partial \alpha_p \rho_p \vec{v}_p}{\partial t} + \nabla \cdot (\alpha_p \rho_p \vec{v}_p \vec{v}_p) = \alpha_p \rho_p \vec{g} - \alpha_p \nabla p_l + K(\vec{v}_l - \vec{v}_p) - \nabla p_p + \nabla \cdot (\alpha_p \bar{\bar{\tau}}_p') \tag{19}$$

$$\frac{\partial \alpha_g \rho_g \vec{v}_g}{\partial t} + \nabla \cdot (\alpha_g \rho_g \vec{v}_g \vec{v}_g) = \alpha_g \rho_g \vec{g} - \nabla p_g + \nabla \cdot (\alpha_g \bar{\bar{\tau}}_g') \tag{20}$$

In Eqs. 18–19, the classical decomposition for the solid pressure (p_p) and that of the surrounding fluid (p_l) was adopted in Newtonian regime, see for example Passalacqua and Fox.[8] Similarly, the average interfacial momentum source is modeled as the drag function, denoted by K, which is not determinant for the development of the numerical procedure, as pointed out by Passalacqua and Fox.[8] In addition, the model includes the gas pressure p_g and the stresses $\bar{\bar{\tau}}_k'$ of each phase, given for the fluid phases by

$$\bar{\bar{\tau}}_l' \equiv \mu_l \left[\nabla \vec{v}_l + (\nabla \vec{v}_l)^T\right], \quad \bar{\bar{\tau}}_g' \equiv \mu_g \left[\nabla \vec{v}_g + (\nabla \vec{v}_g)^T\right] \tag{21}$$

where μ_l and μ_g are the liquid and gas dynamic viscosity, respectively. Notice that the momentum source for the gas phase has been neglected , which is consistent with vanishing surface tension and the presence of a thin (or sharp) interface between the liquid-particle suspension and the atmosphere.

The mathematical model and numerical formulation proposed in this work do not constraint the solid stress term $\bar{\bar{\tau}}_p'$ and solid pressure p_p that characterize particle interactions of flowing suspensions in Newtonian regime and must be elected appropriately depending on the flow regime to compute. On the other hand, the particle pressure p_p and solid stresses $\bar{\bar{\tau}}_p'$ are key to ensure a stable numerical solution procedure in the frictional or quasi-static regime which is dominant during the stopping phase of a mixture flow[16–19] but the study of such rheological regime lies outside the scope of the current work. For the sake of the simplicity, closure laws valid for flowing suspensions in Newtonian regime are used thereafter, see Chang and Powell[1] and Stickel and Powell.[20] Alternatively, the implementation of rheological models based on granular energy proposed by Passalacqua and Fox,[8] van Wachem et al.,[9,10] and Gidaspow,[18] among others, is straightforward.

To obtain the momentum balance equation of the mixture, we add Eqs. 18–20. Taking into account that $\alpha_g = 1 - \gamma$, $\alpha_p = \beta$, $\alpha_l = \gamma - \beta$, and (6), the left-hand side (LHS) of the mixture momentum equation $\vec{C}$ reads

$$\vec{C} \equiv \frac{\partial \rho \vec{v}}{\partial t} + \nabla \cdot \bar{\bar{J}} \tag{22}$$

where $\bar{\bar{J}}$ is the resultant (total) momentum flux associated with the averaged phase velocities

$$\bar{\bar{J}} \equiv \beta \rho_p \vec{v}_p \vec{v}_p + (\gamma - \beta)\rho_l \vec{v}_l \vec{v}_l + (1-\gamma)\rho_g \vec{v}_g \vec{v}_g \tag{23}$$

Using Eqs. 6–12, $\bar{\bar{J}}$ can be recast into the form

$$\bar{\bar{J}} = \rho \vec{v}\vec{v} + \beta\left(1 - \frac{\beta}{\gamma}\right)\frac{\rho_l \rho_p}{\rho_m}\vec{v}_r \vec{v}_r + \gamma(1-\gamma)\frac{\rho_m \rho_g}{\rho}\vec{v}_{r\gamma}\vec{v}_{r\gamma} \tag{24}$$

in which $\vec{v}_{r\gamma}$ denotes the slip velocity between the dense suspension and the air

$$\vec{v}_{r\gamma} \equiv \vec{v}_m - \vec{v}_g = \vec{u}_{r\gamma} + \frac{\beta}{\gamma} s \frac{\gamma - \beta}{\gamma + \beta s}\vec{v}_r \tag{25}$$

Subsequently, substituting Eq. 24 into Eq. 22, the LHS of the momentum balance equation is rewritten as

$$\vec{C} = \frac{\partial \rho \vec{v}}{\partial t} + \nabla \cdot (\rho \vec{v}\vec{v}) - \nabla \cdot \bar{\bar{\tau}}'' - \nabla \cdot \bar{\bar{\tau}}''' \tag{26}$$

with

$$\bar{\bar{\tau}}'' \equiv -\beta\left(1 - \frac{\beta}{\gamma}\right)\frac{\rho_l \rho_p}{\rho_m}\vec{v}_r \vec{v}_r \quad \text{and} \quad \bar{\bar{\tau}}''' \equiv -\gamma(1-\gamma)\frac{\rho_m \rho_g}{\rho}\vec{v}_{r\gamma}\vec{v}_{r\gamma} \tag{27}$$

The tensors $\bar{\bar{\tau}}''$ and $\bar{\bar{\tau}}'''$ represent the momentum diffusion due to the relative motion of solid particles with respect to liquid and of the solid–liquid mixture with respect to air, respectively. Therefore, they are referred hereafter to as "diffusion stress terms." Notice that Min and Kim[5] neglected both terms

in their Eq. 5, which is a valid assumption when slip velocities vanish, that is, under equilibrium. However, these tensors are retained in the current formulation to study unsteady flows. So, the mixture momentum equation can be expressed as

$$\frac{\partial \rho \vec{v}}{\partial t} + \nabla \cdot (\rho \vec{v}\vec{v}) = \rho \vec{g} - \nabla p + \nabla \cdot (\bar{\bar{\tau}}' + \bar{\bar{\tau}}'' + \bar{\bar{\tau}}''') \tag{28}$$

where the mixture pressure is given by

$$p \equiv p_l + p_g + p_p \tag{29}$$

and the bulk laminar stress tensor is denoted by $\bar{\bar{\tau}}' \equiv \sum_{k=\{l,p,g\}} \alpha_k \bar{\bar{\tau}}'_k$.

For a thin interface between the liquid-particle mixture and the gas phase, the bulk viscosity of the three-phase mixture may be assumed as the arithmetic average of the laminar viscosity of the dense suspension μ_m and of the gas phase μ_g, see for example Sethian and Smereka[21]

$$\mu = \gamma \mu_m + (1 - \gamma)\mu_g \tag{30}$$

The harmonic mean of the viscosities is alternatively used for low-disparity viscosity ratios,[22] that is, $\mu_m/\mu_g \sim O(1)$. In Eq. 30, the dense suspension viscosity can be computed using a Krieger–Dougherty model for viscous regime, see Chang and Powell[1] and Stickel and Powell[20]

$$\mu_m(\beta) = \mu_l \left(1 - \frac{\beta}{\beta_M}\right)^n \tag{31}$$

in which β_M is the lowest stable packing of particles and $n = -2$. Subsequently, the shear rate $\dot{\gamma}$ and the bulk laminar stress tensor $\bar{\bar{\tau}}'$ are given by

$$\dot{\gamma} \equiv \sqrt{2}|\bar{\bar{\gamma}}| \quad \text{with} \quad |\bar{\bar{\gamma}}| := (\bar{\bar{\gamma}} : \bar{\bar{\gamma}})^{1/2}, \qquad \bar{\bar{\gamma}} = \frac{1}{2}\left[\nabla \vec{v} + (\nabla \vec{v})^T - \frac{2}{3}(\nabla \cdot \vec{v})\bar{\bar{I}}\right] \tag{32}$$

$$\bar{\bar{\tau}}' \equiv \sum_{k=\{l,p,g\}} \alpha_k \bar{\bar{\tau}}'_k = 2\,\mu\,\bar{\bar{\gamma}} \tag{33}$$

The system of partial differential Eqs. 10 and 28 together with the algebraic relation (13), constitutes a saddle point problem whose solution is the mixture unknowns ($\vec{u}$,p), or ($\vec{v}$,p). Notice that the mixture pressure plays the same role as for single incompressible fluids, that is, to ensure the mixture continuity constraint (10), because $\vec{u}$ is a divergence free vector. Furthermore, the mixture saddle point problem is coupled with the particle momentum Eq. 19 by means of the particle diffusion stress term $\bar{\bar{\tau}}''$. To evaluate $\bar{\bar{\tau}}''$ one can follow two approaches: first, the full Eulerian model that computes the slip velocity $\vec{v}_r$ from the momentum balance equations of the liquid (18) and particles (19) (see Appendix A); second, the algebraic drift-flux model which is valid when the inertia of the particles with respect to the liquid is low.[23–29] Because this work is aimed at presenting and checking the finite volume method described in the section entitled the Finite Volume Discretisation and Solution Procedure, the drift-flux model that is computationally less expensive is adopted from now on.

Drift-flux model

Algebraic closure laws are usually used to compute the slip velocity $\vec{v}_r$ when the relative particle inertia is small, see for example Min and Kim.[5] This approach is known as algebraic slip or mixture model.[11] Timberlake and Morris[4] quantified the migration of particles in gravity-driven free-surface flow of a suspension of neutrally buoyant particles down an inclined plane neglecting liquid and particle inertia. Acrivos and coworkers studied the viscous resuspension of a Hagen–Poiseuille flow[24,25] and sedimentation on inclined surfaces and settlers[23,26] by means of sedimentation fluxes[28] ($\vec{v}_s$), diffusion caused by concentration gradients[27] ($\vec{v}_d$), and shear-induced self-diffusion[29] ($\vec{v}_{sh}$). All these fluxes, that is, $\vec{v}_s$, $\vec{v}_d$, and $\vec{v}_{sh}$, are algebraic relations that allow to compute the particle-liquid slip velocity as

$$\vec{v}_r = \begin{cases} (\vec{v}_s + \vec{v}_d + \vec{v}_{sh})/(1-\beta) & \text{if } \beta < \beta_M \\ 0 & \text{if } \beta \geq \beta_M \end{cases} \tag{34}$$

The main advantage of the algebraic slip model is obviously that requires less computational resources than the full Eulerian approach or the suspension balance model.[30]

Several constitutive laws have been proposed for the average settling velocity of solid particles in still liquids.[1,20,31] For the sake of consistency with similar works, the following expressions given by Richardson and Zaki[1,31] and Acrivos and coworkers,[23–29] respectively, can be used

$$\vec{v}_s = \frac{d^2}{18\mu_l}(1-\beta)^5(\rho_p - \rho_l)\vec{g} \tag{35}$$

$$\vec{v}_s = \frac{d^2}{18\mu_m}\beta(1-\beta)(\rho_p - \rho_l)\vec{g} \tag{36}$$

where d is the solid particle diameter.

In the presence of a concentration gradient along the perpendicular to the streamwise direction, Leighton and Acrivos[27] have shown that the Fickian diffusive flux associated with particles of radius $a = d/2$ can be written as

$$\vec{v}_d = -D_d \nabla \beta \tag{37}$$

where the dimensionless form of the diffusion coefficient is

$$\widehat{D}_d \equiv \frac{D_d}{a^2\dot{\gamma}} = \frac{1}{3}\beta^2\left(1 + \frac{1}{2}e^{8.8\beta}\right) + 0.6\beta^2\frac{1}{\mu}\frac{d\mu}{d\beta} \tag{38}$$

Furthermore, when the particle flux due to gradients in the shear stress cannot be neglected a new contribution to the diffusive flux appears,[29] given by

$$\vec{v}_{\mathrm{sh}} = -D_{\mathrm{sh}}\nabla\dot{\gamma} \quad \text{with} \quad \widehat{D}_{\mathrm{sh}} \equiv \frac{D_{\mathrm{sh}}}{a^2} = 0.6\beta^2 \tag{39}$$

Morris and Brady[32] and Morris and Boulay[33] used the suspension balance model to show that the shear-induced self-diffusion velocity arises from the particle normal stresses (particle pressure and normal stress differences), playing a fundamental role in particle migration.

Finite Volume Discretization and Solution Procedure

In this section, a segregated FVM is proposed to solve for the hyperbolic scalar transport equation of γ (14) and β (16), the mixture continuity equation (10) and the mixture momentum balance equation (28). Including the equation for $\vec{v}_r$ (34) is straightforward. All these equations are said to be in

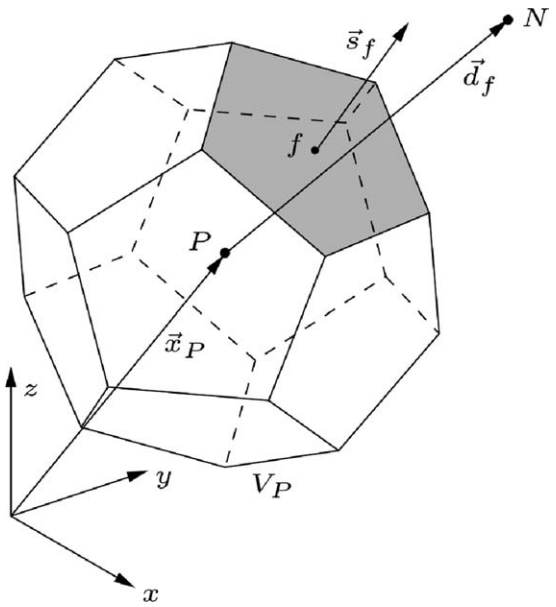

Figure 2. Computational cell.

"strong conservation form" due to the fact that all terms have the form of the divergence of a vector or tensor as described by Patankar[34] and Ferziger and Perić.[35] The use of the strong conservation form of the equations together with the FVM automatically insures global conservation. For that reason, special attention has been paid to the mathematical formulation of the problem under consideration in the section entitled Formulation of the Problem, retaining this property. Furthermore, to preserve global conservation in the numerical solution, a fixed direction coordinate system (i.e., Cartesian components) is adopted in this work.

The first equation (14) introduces several difficulties in the numerical problem because the function γ is sharp at the interface and is bounded between 0 and 1, see Gopala and van Wachem.[7] Similarly, the unknown β of the second equation (16) may exhibit discontinuities[36] and is bounded by 0 and β_M. The numerical solution obtained with low order methods is usually diffusive, smearing, therefore, the interface, while high order schemes may exhibit spurious oscillations.[15] Therefore, special care is required to guarantee a sharp and bounded solution, as described below. The last two equations, (10) and (28), constitute a saddle point problem whose solution is the volumetric mixture velocity $\vec{\boldsymbol{u}}$ (or $\vec{\boldsymbol{v}}$) and the mixture pressure p ensuring the incompressible constraint (10). For doing this, the iterative Pressure Implicit with Splitting of Operators (PISO) algorithm[34,35] is adopted here and the pressure equation is derived as the Schur complement. Recall that $\vec{u}$ and $\vec{v}$ are related by the algebraic equation (13), where the particle-liquid relative velocity $\vec{\boldsymbol{v}}_{\boldsymbol{r}}$ (34) is evaluated hereafter by means of the algebraic slip velocities for the sake of comparison with previous works.

Unknown dependent variables to be computed are stored at the cell centroid $\vec{x}_P$, using thus the so-called collocated arrangement, $\int_{V_P}(\vec{x} - \vec{x}_P)\, dV = 0$, where cell volume is denoted by V_P. The main advantage of this approach is the reliability of handling with complicated solution domains. However, to overcome the main disadvantage of the collocated arrangement, that is the occurrence of oscillations in the pressure, an oscillation-free pressure-velocity coupling in line with Rhie and Chow[37] is adopted. Figure 2 shows an example of the convex polyhedral cell, whose boundaries are composed of a set of convex polygons, although in the present work hexahedral cells are used. Each cell has a neighboring cell across each of its faces, of centroid denoted by N, and positional vector relative to $\vec{x}_P$ for the face f defined as $\vec{d}_f = \vec{x}_N - \vec{x}_P$. Similarly, using the centroid rule, the face center, $\vec{x}_f$, is given by $\int_{S_f}(\vec{x} - \vec{x}_f)\, dS = 0$. Next, the face area vector $\vec{s}_f$ is a surface normal vector whose magnitude is equal to the area of the face. The face area is calculated from the integrals $\vec{s}_f = \int_{S_f} \vec{n}\, dS$. When operating on a single cell, it is assumed that all face area vectors $\vec{s}_f$ point outward of cell P.

Numerical discretization of differential operators were implemented up to second-order accuracy in space and time by postulating a linear spatial (and temporal) variation of unknown quantities, for example

$$\gamma(\vec{x}, t) = \gamma_P + (\vec{x} - \vec{x}_P) \cdot (\nabla\gamma)_P \tag{40}$$

$$\gamma(\vec{x}, t + \Delta t) = \gamma^t + \Delta t \left(\frac{\partial \gamma}{\partial t}\right)^t \tag{41}$$

where $\gamma^t \equiv \gamma(\vec{x},t)$, $\gamma_P \equiv \gamma(\vec{x}_P,t)$, and Δt is the time step. For a detailed description of the numerical discretization of the differential operator in collocated meshes (rate of change term, gradient operator, convection operator, diffusion operators as well as source and sink terms) the reader is referred to the work by Patankar,[34] Ferziger and Perić,[35] and Jasak,[38] among others. A sketch of the numerical strategy is given in Table 1 and only the innovative parts of the algorithm are introduced below, in particular the segregated explicit FVM and the extension of the PISO algorithm.

To fulfill a sharp and bounded solution to γ (14) and β (16), an explicit method particularly designed for scalar transport equations[40] is used. Similar schemes were used with success by the author[41] to solve for system of hyperbolic balance laws with source terms. To start the normal flux of γ at time t is computed as

$$\phi_\gamma^t \equiv \left[\gamma\vec{u} + \gamma(1-\gamma)\vec{u}_{r\gamma}\right]_f^t \cdot \vec{s}_f = \gamma_f^t[\phi_u + (1-\gamma_f)\phi_{r\gamma}]^t \tag{42}$$

where the normal convective flux is given by $\phi_u^t \equiv \vec{u}_f^t \cdot \vec{s}_f$ and $\phi_{r\gamma}^t \equiv (\vec{u}_{r\gamma})_f^t \cdot \vec{s}_f$. The solution to (14) is obtained

Table 1. Numerical Solution Procedure

1 Update the normal flux ϕ_γ^t (42) and compute $\gamma^{t+\Delta t}$ by solving explicitly for the scalar transport equation (14).
2 Update the normal flux ϕ_β^t (43) and compute $\beta^{t+\Delta t}$ by solving explicitly for the scalar transport equation (16).
3 Update the normal flux of mixture mass $(\rho\phi)^t$ from (44).
4 Compute the mixture density $\rho^{t+\Delta t}$ from (45).
5 Discretise the momentum balance equation (47) and assemble the algebraic system of equations (48)–(50).
6 Predict the velocity field $\vec{v}^*$ by solving for (54) (with $\hat{p}^{t+\Delta t} \approx \hat{p}^t$.
7 Solve for (48)–(50) subject to the incompressible constraint (53):
  a Predict convective flux $\phi^* = \vec{v}^* \cdot \vec{s}_f$ using equation (57).
  b Construct the pressure equation (56) and solve for the reduced pressure $\hat{p}^*$.
  c Repeat (a)–(b) until convergence of the residuals.
8 $\hat{p}^{t+\Delta t} = \hat{p}^*$ and the velocity field $\vec{v}^{t+\Delta t}$ from the reconstructed value of flux correction[8,39].
9 Compute $\vec{v}_r^{t+\Delta t}$ from (34), and repeat 7–9 up to convergence.
10 Update flow properties (viscosity, etc).
11 Update the volumetric flux ϕ_u & the new time step, (58) and (61).

straightforward by limiting the flux ϕ_γ^t, hereafter denoted by $\tilde{\phi}_\gamma^t$, which is used to compute $\gamma^{t+\Delta t}$, see Zalesak.[40] So the normal flux of β is expressed as a function of the limited flux $\tilde{\phi}_\gamma^t$. Taking into account (17) and (42), it yields

$$\phi_\beta^t \equiv \left[\beta\vec{u} + \beta(1-\beta)\vec{u}_{r\beta}\right]_f^t \cdot \vec{s}_f = \beta_f^t \left[\frac{\tilde{\phi}_\gamma}{\gamma_f} + \left(1 - \frac{\beta_f}{\gamma_f}\right)\phi_r\right]^t \tag{43}$$

where $\phi_r^t \equiv (\vec{v}_r)_f^t \cdot \vec{s}_f$. Then, (16) is solved following the same procedure as for (14), providing for $\beta^{t+\Delta t}$ as a function of β^t and ϕ_β^t. Consequently, taking into account (12) and (17), the normal flux of mass $\rho\vec{v}$ (6) at the cell faces can be determined from the normal (limited) flux of γ (42) and β (43) as

$$(\rho\phi)^t \equiv (\rho\vec{v})_f^t \cdot \vec{s}_f = \rho_g \phi_u^t + (\rho_p - \rho_l)\tilde{\phi}_\beta^t + \left[(\rho_m - \rho_g) - \frac{\beta}{\gamma}(\rho_p - \rho_l)\right]_f^t \tilde{\phi}_\gamma^t \tag{44}$$

Hence, the mixture density ρ at $t + \Delta t$ is given by (5)

$$\rho^{t+\Delta t} = \rho_p \beta^{t+\Delta t} + \rho_l(\gamma^{t+\Delta t} - \beta^{t+\Delta t}) + \rho_g(1 - \gamma^{t+\Delta t}) \tag{45}$$

Now the momentum balance equation (28) is solved subject to the incompressible constraint (10). As usual,[34,35] the reduced pressure $\hat{p}$ is given by

$$\hat{p} \equiv p - \rho\vec{g} \cdot \vec{x} \tag{46}$$

and, thus (28) yields

$$\frac{\partial \rho\vec{v}}{\partial t} + \nabla \cdot (\rho\vec{v}\vec{v}) = -\nabla\hat{p} - \vec{g} \cdot \vec{x}\nabla\rho + \nabla \cdot (\bar{\bar{\tau}}' + \bar{\bar{\tau}}'' + \bar{\bar{\tau}}''') \tag{47}$$

The momentum equation (47) is discretized using a first-order accurate time integrator with the non-linear terms lagged. Then, the mass flux $\rho\phi$ that affects the advection term is discretized explicitly using Eq. 44. In doing so, the limited fluxes $\tilde{\phi}_\gamma^t$ and $\tilde{\phi}_\beta^t$ used to solve for $\gamma^{t+\Delta t}$ and $\beta^{t+\Delta t}$ are accounted for in the pressure-velocity coupling algorithm. The system of algebraic equations arising from the discretization of (47) in cell P can be written as[35,42]

$$\mathcal{A}(\vec{v}^{t+\Delta t}; \vec{v}^t) = -\vec{g} \cdot \vec{x}\,\nabla\rho^{t+\Delta t} - \nabla\hat{p}^{t+\Delta t} \tag{48}$$

For instance, for a first-order explicit Euler integrator, $\mathcal{A}$ is defined as follows

$$\mathcal{A} := \frac{V_P}{\Delta t}\left[(\rho_P^{t+\Delta t}\vec{v}_P^{t+\Delta t} - (\rho\vec{v})_P^t\right] + \sum_f (\rho\phi)^t \vec{v}_f^{t+\Delta t} - \sum_f \mu_f^t \vec{s}_f \cdot (\nabla\vec{v})_f^{t+\Delta t} - \mathcal{R}^{eff\mathcal{C}} \tag{49}$$

where subscripts P and f denotes that the magnitudes are evaluated at the cell centroid $\vec{x}_P$ and the cell face f, respectively, $\sum_f$ denotes sum over the cell faces, and the Reynolds stress correction term $\mathcal{R}^{eff\mathcal{C}}$ is given by

$$\mathcal{R}^{eff\mathcal{C}} = \sum_f (\mu^t)_f \vec{s}_f \cdot \left[(\nabla\vec{v})^T - \frac{2}{3}(\nabla \cdot \vec{v})\bar{\bar{I}}\right]_f^t - \sum_f \vec{s}_f \cdot (\bar{\bar{\tau}}'' + \bar{\bar{\tau}}''')_f^t \tag{50}$$

Notice that $\mathcal{R}^{eff\mathcal{C}}$ is handled explicitly to avoid the coupling of the velocity components, which eases the numerical implementation.

The velocity $\vec{v}_f^{t+\Delta t}$ on the LHS of (49) is interpolated linearly,[35,42] as a function of $\vec{v}_P^{t+\Delta t}$ and its nearest neighbor $\vec{v}_{nb}^{t+\Delta t}$. Reformulating (48)–(50) in terms of $\vec{v}_P$ and $\vec{v}_{nb}$, $\mathcal{A}$ can be decomposed into a matrix containing its diagonal coefficients, $\mathcal{A}_D$, plus the off-diagonal coefficients, $\mathcal{A}_N$, and the source vector $\mathcal{A}_S$

$$\mathcal{A}_D\vec{v}_P^{t+\Delta t} = \mathcal{A}_S - \mathcal{A}_N\vec{v}_{nb}^{t+\Delta t} - \vec{g} \cdot \vec{x}\,\nabla\rho^{t+\Delta t} - \nabla\hat{p}^{t+\Delta t} \tag{51}$$

This classical decomposition is useful to formulate a Jacobi iteration scheme, see Ferziger and Perić,[35] and facilitates the solution of the semidiscretized form of the momentum equation, as described below.

The pressure-velocity coupling is formulated based on the continuity equation (10). Rewriting Eq. 10 in terms of the mean velocity $\vec{v}$ (13), and evaluating it in the cell centroid $\vec{x}_P$ at $t + \Delta t$, one has

$$\nabla \cdot \vec{v}_p^{t+\Delta t} = \nabla \cdot \left[\gamma(1-\gamma)\frac{\rho_m - \rho_g}{\rho}\vec{u}_{r\gamma} + \beta s\frac{\gamma - \beta}{\gamma + \beta s}\frac{\rho_m}{\rho}\vec{v}_r\right]_P^{t+\Delta t} \tag{52}$$

Next, writing Eqs. 51–52 in compact form

$$\begin{bmatrix} \mathcal{A}_D & \nabla \\ \nabla\cdot & 0 \end{bmatrix}\begin{bmatrix} \vec{v}_p^{t+\Delta t} \\ \hat{p}^{t+\Delta t} \end{bmatrix} = \begin{bmatrix} \mathcal{A}_S - \mathcal{A}_N\vec{v}_{nb}^{t+\Delta t} - \vec{g} \cdot \vec{x}\,\nabla\rho^{t+\Delta t} \\ \nabla \cdot \left[\gamma(1-\gamma)\frac{\rho_m - \rho_g}{\rho}\vec{u}_{r\gamma} + \beta s\frac{\gamma-\beta}{\gamma+\beta s}\frac{\rho_m}{\rho}\vec{v}_r\right]_P^{t+\Delta t} \end{bmatrix} \tag{53}$$

and solving for $\vec{v}_P$ and $\hat{p}$ yields

$$\vec{v}_P^{t+\Delta t} = \frac{1}{\mathcal{A}_D}\left[\mathcal{A}_S - \mathcal{A}_N\vec{v}_{nb}^{t+\Delta t}\right] - \frac{1}{\mathcal{A}_D}\left[\vec{g} \cdot \vec{x}\,\nabla\rho + \nabla\hat{p}\right]_P^{t+\Delta t} \tag{54}$$

$$\nabla \cdot \left[\frac{1}{\mathcal{A}_D}\nabla\hat{p}\right]_P^{t+\Delta t} = \nabla \cdot \vec{v}_p^{t+\Delta t} - \nabla \cdot \left[\gamma(1-\gamma)\frac{\rho_m - \rho_g}{\rho}\vec{u}_{r\gamma} + \beta s\frac{\gamma-\beta}{\gamma+\beta s}\frac{\rho_m}{\rho}\vec{v}_r\right]_P^{t+\Delta t} \tag{55}$$

Obviously (54) and (55) are coupled and were solved iteratively using a Jacobi iteration scheme similar to PISO.[34,35] First, the available pressure field from previous time step $\hat{p}^* = \hat{p}^t$ is used (first iteration), which is updated during the corrector stage $\hat{p}^*$ (later iterations). Conservative fluxes $\phi^* \equiv \vec{v}^* \cdot \vec{s}_f$ corresponding to $\hat{p}^*$ are also available. Then the momentum equation $\mathcal{A}$ (48) is discretised and the momentum equation (54) is solved using the guessed pressure, that is, doing $\hat{p}^{t+\Delta t} \approx \hat{p}^*$ on the right-hand side (RHS) of (48) and (54). This step is called momentum predictor and updates the value of $\vec{v}^*$. Subsequently, integrating Eq. 55 in the computational cell and taking into account Gauss' theorem, one has

$$\sum_f \vec{s}_f \cdot \left[\left(\frac{1}{\mathcal{A}_D}\right)_f (\nabla\hat{p}^*)_f\right] = \sum_f \phi^* - \vec{s}_f \cdot \left[\gamma(1-\gamma)\frac{\rho_m - \rho_g}{\rho}\vec{u}_{r\gamma} - \beta s\frac{\gamma-\beta}{\gamma+\beta s}\frac{\rho_m}{\rho}\vec{v}_r\right]_f^{t+\Delta t} \tag{56}$$

Thus, the new pressure $\hat{p}^*$ is calculated from Eq. 56 based on the actual value of ϕ^*. This is called pressure correction step. The pressure equation (56) is a Poisson equation with the diagonal part of the discretized momentum acting as diffusivity and the divergence of the velocity on the RHS. The block $\mathcal{A}_D$ only contains diagonal entries and is easy to invert, preserving the sparseness pattern in the triple product.

Based on the new pressure solution $\hat{\boldsymbol{p}}^*$, conservative face flux ϕ^* ($\equiv \vec{\boldsymbol{v}}^* \cdot \vec{\boldsymbol{s}}_f$) are updated from (54)

$$\phi^* = \left(\frac{\mathcal{A}_S - \mathcal{A}_N \vec{v}^*_{nb}}{\mathcal{A}_D}\right)_f \cdot \vec{s}_f - \left(\frac{1}{\mathcal{A}_D}\right)_f \left[(\vec{g}\cdot\vec{x})_f |\vec{s}_f| \nabla_f^{\perp} \rho^{t+\Delta t} + |\vec{s}_f| \nabla_f^{\perp} \hat{p}^*\right] \quad (57)$$

and iterate (56) and (57) up to reach a converged solution. Here the face normal gradient is denoted by $\nabla_f^{\perp}$ and is computed as the inner product of the face gradient ∇_f and unit normal to the face $\vec{n}_f$, for example $\nabla_f^{\perp}\ \rho \equiv \vec{n}_f \cdot \nabla_f \rho$. To conclude, cell-centered velocities are obtained from the corrected flux field ϕ^* using a reconstruction procedure in such a way that pressure-velocity decoupling cannot occur, see section 3.2.10 in Rusche.[39] So, $\vec{v}_P^{t+\Delta t}$ is evaluated replacing the term $[\vec{g}\cdot\vec{x}\,\nabla\rho + \nabla\hat{p}]$ in (54) with the reconstructed value of the flux correction, see point 5 in section 4 by Passalacqua and Fox,[8] and is merely regarded as a secondary variable used to compute $\vec{v}_r^{t+\Delta t}$ from (34). Alternatively, it could be corrected in an explicit manner, evaluating (54), as a consequence of the new pressure distribution, see section 3.8.2.1 in Jasak[38] and section 3.2.9 in Rusche.[39] However, the reconstruction approach is needed when the flow exhibits regions where the phase fractions changes abruptly and the densities are very different. The cycle (48)–(57) is repeated up to convergence of $p^{t+\Delta t}$, $\vec{v}^{t+\Delta t}$, and $\vec{v}_r^{t+\Delta t}$.

Once the pressure (56) and velocity (57) equations are iterated until convergence, the volumetric flux ϕ_u is updated from (13)

$$\phi_u^{t+\Delta t} = \phi^{t+\Delta t} - \left[\gamma(1-\gamma)\frac{\rho_m - \rho_g}{\rho}\right]_f^{t+\Delta t} \phi_{r\gamma}^{t+\Delta t} - \left[s\beta\tfrac{\gamma-\beta}{\gamma+\beta s}\tfrac{\rho_m}{\rho}\right]_f^{t+\Delta t} \phi_r^{t+\Delta t} \quad (58)$$

The forward explicit scheme in time imposes a Courant–Friedrichs–Lewy (CFL) stability restriction on the time step Δt, which is calculated and adjusted during the numerical simulation. On the one hand, the Courant number corresponding to (14) is defined as

$$\mathrm{CFL}_\gamma = \frac{|\vec{u}_f \cdot \vec{s}_f|}{\vec{d}_f \cdot \vec{s}_f}\Delta t \quad (59)$$

In the above definition, the influence of the compression velocity $\vec{u}_{r\gamma}$ is neglected because we shall analyze flows in the absence of gas–liquid mixing. On the other hand, the Courant number of (16) accounts for the relative velocity $\vec{u}_{r\beta}$. For this reason, a second Courant number is introduced based on the effective velocity $\vec{u} + (1+\beta)\vec{u}_{r\beta}$

$$\mathrm{CFL}_\beta = \frac{|[\vec{u} + (1+\beta)\vec{u}_{r\beta}]_f \cdot \vec{s}_f|}{\vec{d}_f \cdot \vec{s}_f}\Delta t \quad (60)$$

Thus, one can define the maximum local Courant number $\mathrm{CFL}_o = \max\{\mathrm{CFL}_\beta, \mathrm{CFL}_\gamma\}$ from (59)–(60) at the current time step, which is adjusted to run the next iteration according to the following relation[43]

$$\Delta t \leftarrow \min\left\{\frac{\mathrm{CFL}_{\max}}{\mathrm{CFL}_o}\Delta t, \left(1 + \lambda_1 \frac{\mathrm{CFL}_{\max}}{\mathrm{CFL}_o}\right)\Delta t, \lambda_2 \Delta t\right\} \quad (61)$$

in which $\mathrm{CFL}_{\max}$ is the desired Courant number, $\lambda_1 = 0.1$ and $\lambda_2 = 1.2$ are damping factors used to avoid numerical instabilities arising from time step oscillations.

Results

Numerical results are presented in this section for a series of benchmarks which progressively validate different aspects of the whole algorithm. First the settling of a homogeneous suspension initially at rest on a horizontal boundary is analyzed. This benchmark serves to show the shock capturing capabilities of the numerical algorithm because such flow exhibits discontinuities in the solid volumetric concentration β. Next, the viscous resuspension phenomenon is illustrated by considering shear-induced self-diffusion of particles. The solution from this section is subsequently used as boundary condition to study the shape of the tip region of a uniform stream down an inclined plane. The capabilities of the proposed model to solve accurately for the advancing of a wetting front, to obtain the non-hydrostatic pressure distribution and the non-uniform velocity field within the tip region are illustrated with the latter examples. Finally, it is shown that the model is also able to predict the developments of free surface instabilities, as viscous roll waves, in uniform flows down sloping beds.

In the applications, advective fluxes at velocities of $\vec{u}$ and $\{\vec{u}_{r\gamma}, \vec{v}_r\}$ through cell faces were evaluated by means of van Leer[44] and quartic compression[45] schemes, respectively. Next, ϕ_γ (42) and ϕ_β (43) were limited with Multidimensional Universal Limiter with Explicit Solution, developed by OpenCFD Ltd.[46,47] Grid convergence tests were performed for each problem though wont be reported for the sake of the brevity.

Vertical settler

Homogeneous concentrated suspensions of non-Brownian solid particles and Newtonian liquids may develop complex flow fields due to the growth of localized velocity fluctuations.[48] However, macroscopic properties such as the locations of bottom and top interfaces developing during the settling of quasi-monodisperse suspensions are successfully predicted using simple constitutive relations for the bulk viscosity $\mu_m(\beta)$ and average sedimentation velocities $\vec{v}_s$, see Chang and Powell,[1] Snabre et al.,[48] and Mills and Snabre.[49] So the use of mixture or drift-flux model has become a useful tool to analyze the behavior of suspensions from dilute to concentrated regime in vertical settlers.

Here, numerical results are compared successfully with experimental results from the "Settling of quasi-monodisperse suspensions" section in Snabre et al.[48] The physical properties of the solid and liquid phases they used are $\rho_p = 1190$ kg m^{-3}, $d = 0.19$ mm, $\beta_M = 0.57$, $\rho_f = 890$ kg m^{-3}, and $\mu_f = 0.025$ kg m^{-1} s^{-1}. The computational domain is described by a structured mesh with $1 \times 1 \times 1000$ cells ($X \times Y \times Z$) and mesh size of $\Delta X = \Delta Y = \Delta Z = 1.2 \times 10^{-4}$ m. Initial conditions are given by

$$\gamma(z)=1,\quad \beta(z)=\begin{cases}\beta_o & \text{if } 0\le z\le 0.1\text{ m}\\ 0 & \text{if } 0.1<z\le 0.12\text{ m}\end{cases}$$

$$\vec{v}(z)=\vec{u}(z)=0,\quad \hat{p}(z)=0 \quad (62)$$

in which the initial volumetric concentration of solid particles is $\beta_o = 0.4$. As boundary condition, periodic flow is imposed for all variables over all boundaries except at the bottom ($z = 0$ m) and top ($z = 0.12$ m), where

$$\gamma=1,\quad (\nabla\beta)\cdot\vec{n}=0,\quad \vec{v}=\vec{u}=0,\quad (\nabla\hat{p})\cdot\vec{n}=0 \quad (63)$$

The thick dashed line in Figure 3a corresponds with the vertical profile of $\beta(z)$ (62) at the initial instant of time, where a discontinuity at $z = 0.1$ m is readily observed. Solid particles settle as time increases and, hence, the top interface separating the clear water and dense suspension regions moves downward up to, approximately, 1600 s. Obviously, the top interface velocity is given by $V = |\vec{v}_s|$ (35). As a consequence, a lower layer grows upward the solid bottom[48,49] ($z = 0$) with velocity $V^* = \beta V/(\beta_M - \beta)$. Following Figure 2c in Snabre et al.,[48] the volumetric concentration β can also be drawn in the phase plane $\{t,z\}$, see Figure 3b. An excellent agreement between current computations and their experimental results is found, which are plotted with filled circles and squares. Furthermore, the shock capturing capability of the implemented algorithm is pointed out, because spurious oscillations (inherent to second-order accurate spatial discretization[50]) did not develop.

Viscous resuspension in uniform flow down an inclined plane

In this section, numerical results illustrating the viscous resuspension phenomenon are shown for a uniform flow down a constant slope bed which is initially homogeneous, see Leighton and Acrivos,[28] among others.[23,26] The initial condition corresponds to the Nusselt flat-film solution on a plane inclined at an angle θ with respect to the horizontal

$$\gamma(z)=1,\quad \beta(z)=\beta_o,$$
$$\vec{v}(z)=\vec{u}(z)=V_s\left[2\frac{z}{h}-\left(\frac{z}{h}\right)^2\right]\vec{e}_x,\quad \hat{p}(z)=0 \quad \text{with} \quad 0\le z\le h \quad (64)$$

where h is the Nusselt film thickness and $V_s = \rho g h^2 \sin\theta/(2\mu_m)$ is the free surface velocity. The vertical profiles of the particle volumetric concentration and of the streamwise velocity are depicted in Figure 4 in dashed line for $\rho_p = 2475$ kg m^{-3}, $d = 0.625$ mm, $\beta_o = 0.3851$, $\beta_M = 0.605$, $\rho_f = 971$ kg m^{-3}, $\mu_f = 0.971$ kg m^{-1} s^{-1}, $h = 10d$ and $\theta = 45°$. For the sake of the completeness, the expression for $\vec{v}_s$ given by Acrivos and coworkers (36) was used.

As boundary condition, periodic flow is imposed for $\{\vec{v}, \vec{u}, \gamma, \beta, \hat{p}\}$ over all boundaries except at the bottom ($z = 0$ m) and top ($z = h$), where

$$\gamma=1,\quad (\nabla\beta)\cdot\vec{n}=0,\quad \vec{v}=\vec{u}=0,\quad (\nabla\hat{p})\cdot\vec{n}=0 \quad \text{at } z=0$$
$$\gamma=1,\quad (\nabla\beta)\cdot\vec{n}=0,\quad (\nabla\vec{v})\cdot\vec{n}=(\nabla\vec{u})\cdot\vec{n}=0,\quad \hat{p}=0 \quad \text{at } z=h \quad (65)$$

Finally, the computational domain is given by a structured mesh with $1 \times 1 \times 100$ cells ($X \times Y \times Z$) and mesh size of $\Delta X = \Delta Y = \Delta Z = 6.25 \times 10^{-5}$ m.

According to Acrivos and coworkers theory,[23,26] there are three possible regimes depending on the relative importance

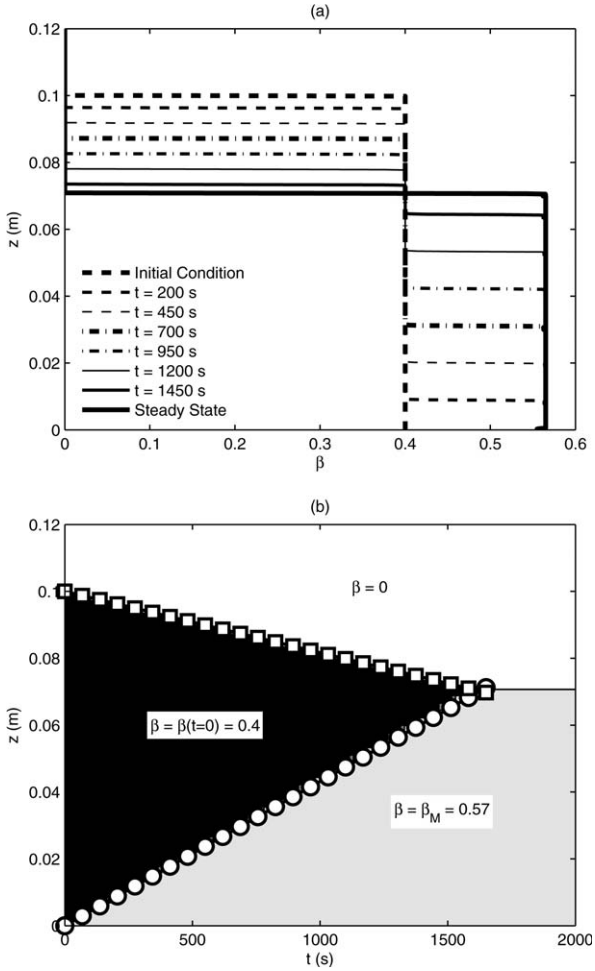

Figure 3. Numerical solution to $\beta(z,t)$ for the experiments by Snabre et al.:[48]

(a) vertical profiles of $\beta(z)$ at several instants of time and (b) solution in the plane $\{t,z\}$. "Squares" and "circles" in panel (b) depict the experimental results for the top and bottom interfaces, respectively, which are in agreement with the shocks arising in the numerical solution.

of the sedimentation ($\vec{v}_s$) with respect to Fickian ($\vec{v}_d$) and shear-induced self-diffusion ($\vec{v}_{sh}$) fluxes in an initial homogeneous mixture, namely: a homogeneous state that corresponds with a mixture in equilibrium, that is, $\beta = \beta_o =$ const and $\vec{v}_s = \vec{v}_{sh} + \vec{v}_d$; the settled and resuspended (or risen) regimes occurring when, in an initial homogeneous mixture, solid particles are out of equilibrium because $|\vec{v}_s|^2 > |(\vec{v}_{sh} + \vec{v}_d)\cdot\vec{v}_s|$ and $|\vec{v}_s|^2 < |(\vec{v}_{sh} + \vec{v}_d)\cdot\vec{v}_s|$, respectively.

It is an easy exercise to show that, for a uniform flow down, a constant slope bed with initial conditions given by (62), there is a critical bed slope θ_c that ensures a homogeneous regime

$$\theta_c = \text{atan}\left[\frac{2(\rho_p-\rho_l)}{\rho_p\beta_o+(1-\beta_o)\rho_l}\frac{(1-\beta_o)}{b\beta_o}\right] \quad (66)$$

in which b is 0.6 when (38) is used,[27] or 0.43 when using Phillips et al.[51] fitting. If $\theta = \theta_c$, then the initial condition (62) prevails at late time. Conversely, solid particles settle when $\theta < \theta_c$. Finally, when $\theta > \theta_c$ solid particles resuspend as described by Acrivos and coworkers.[23,26]

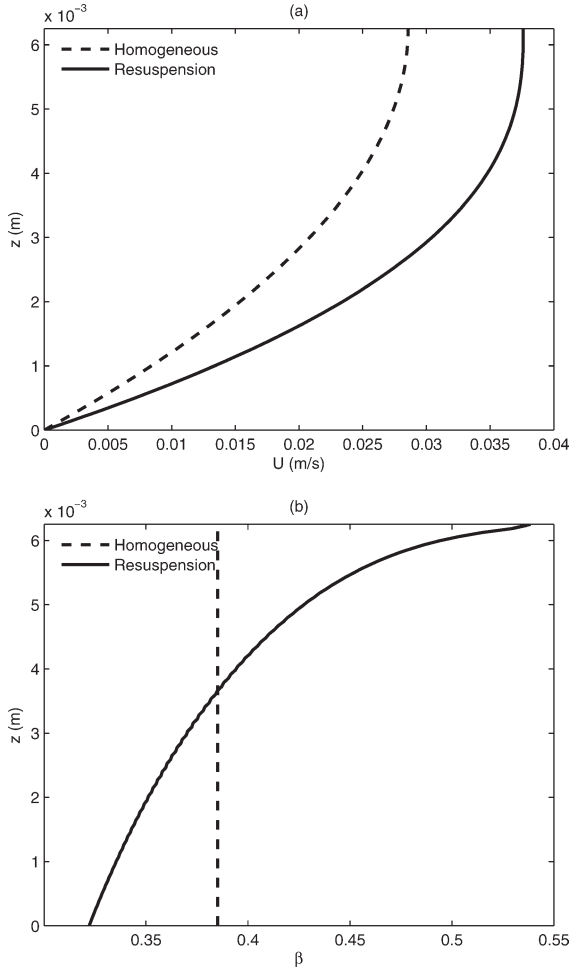

Figure 4. (a) Streamwise velocity and (b) solid volumetric concentration profiles for a homogeneous (dashed line) and resuspended suspension (solid line).

Dashed and solid lines correspond with the initial condition ($t = 0$) and the quasi-steady solution ($t = 1500$ s) employed and obtained, respectively, in the section entitled Viscous resuspension in uniform flow down an inclined plane. The temporal evolution of the solution is also shown in Figure 5.

Substituting the physical properties given above into (66), it yields $\theta_c \approx 30°$. So viscous resuspension must be observed during the numerical simulation because $\theta = 45° > \theta_c$. Indeed, setting the initial and boundary conditions given by (64) and (65), respectively, and including $\vec{v}_d$ (37), $\vec{v}_{sh}$ (39), and $\vec{v}_s$ (36) into $\vec{v}_r$ (34), allowed the development of viscous resuspension in the numerical simulation. Indeed, the streamwise velocity increases as time proceeds (Figure 5a) due to the viscous resuspension of solid particles (see Figure 5b). During the transient stage from $t = 0$ to 60 s the relative velocity $\vec{v}_{\rm sh}$ (39) is very high owing a fast variation of β and $\vec{v}$. However, for $t > 60$ s the relative velocity decreases when the settling flux tends to balance the Fickian and shear-induced self-diffusion fluxes. Therefore, temporal variations of β and $\vec{v}$ are much slower at $t > 60$ s than at earlier time. At late time, that is, $t = 1500$ s, a quasi-steady regime is reached with values of the relative velocity lower than $\max|\vec{v}_r(t = 0)|/10^3$, which can be neglected. These findings are analogous to those reported by Timberlake and Morris[4] for neutrally buoyant particles, who observed non-uniform velocity profiles in the upstream reach of their channel, see their Figure 6, and quasi-uniform profiles further downstream. The ensuing velocity and concentration profiles diverge from the homogeneous case depicted in Figure 4 and agree well with previous theoretical results.[52] A direct comparison between simulations and experiments is difficult in the absence of internal dynamics measurements that require outstanding facilities.[53]

Figure 4 clearly indicates that the solid volumetric concentration monotonously increases with z and that a heavy material flows above a lighter one when migration upward overwhelms settling. This apparently unstable stratification is possible if the material exerts normal stresses that are responsible for particle migration, see the section entitled Drift-flux-model and subsection 4.1 in Morris and Brady,[32] referred thereafter as MB. Using a dimensional argument, see for example Barenblatt,[54] MB defined a dimensionless gravitational parameter B that quantifies the relative influence of buoyancy-driven motion (settling) to shear-driven migration in a horizontal pressure-driven flow

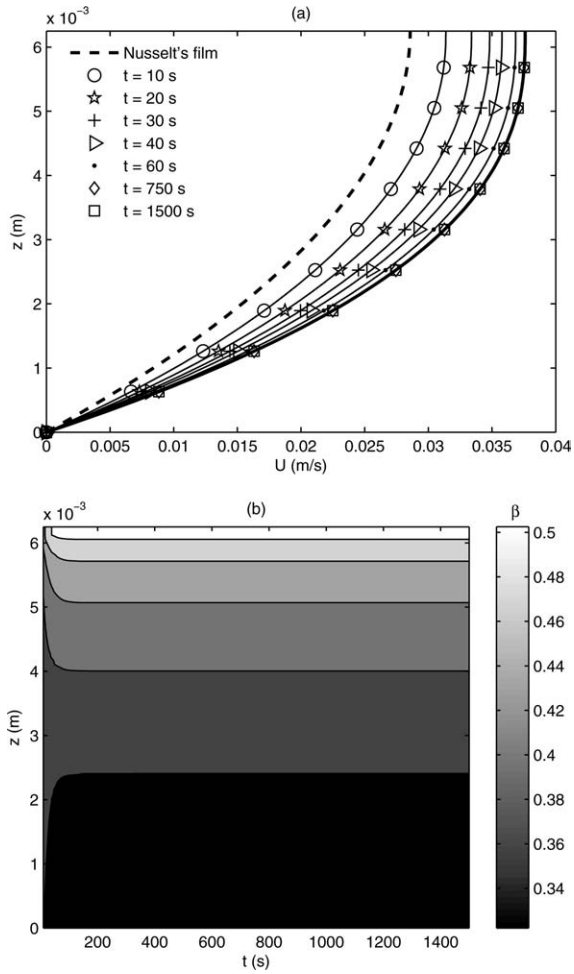

Figure 5. (a) Temporal evolution of the streamwise velocity and (b) solid volumetric concentration for the viscous resuspended suspension described in the section entitled Viscous resuspension in uniform flow down an inclined plane.

The initial condition ($t = 0$) and the quasi-steady solution at $t = 1500$ s are shown in Figure 4 in dashed and solid lines, respectively.

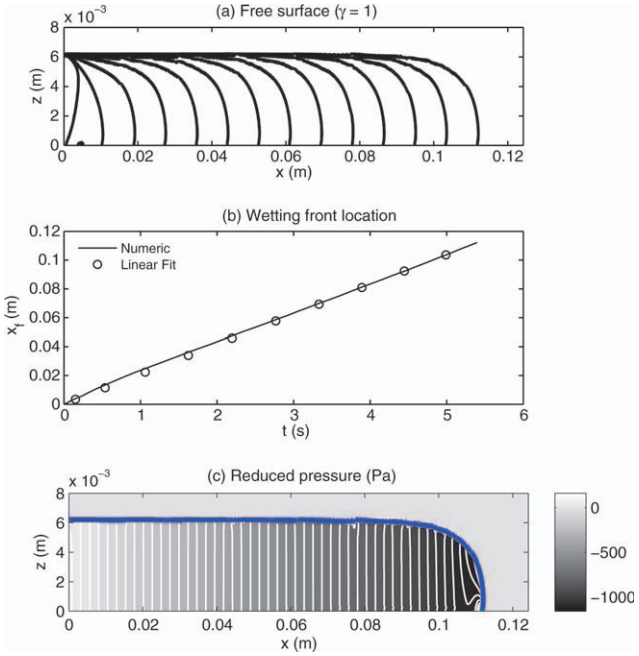

Figure 6. (a) Temporal evolution of the free surface interface for the homogeneous inlet profiles in Figure 4 and $\vec{v}_r = 0$ at $t = 0.15, 0.41, 0.79, 1.20, 1.62, 2.05, 2.5, 2.9, 3.33, 3.75, 4.15, 4.6, 5$, and 5.4 s; (b) location of the wetting front as a function of time; (c) isocontours of the reduced pressure $\hat{p}$ at $t = 5.4$ s.

The thin solid line in (c) highlights the free surface. Aspect ratio in (a) and (c) is 4:1. [Color figure can be viewed in the online issue, which is available at wileyonlinelibrary.com.]

$$B \equiv \left(\frac{v}{V}\right)\left(\frac{h}{a}\right)^2 \tag{67}$$

where $v = 2(\rho_p - \rho_l)\, ga^2/9\mu_m$ is the Stokes settling velocity of an isolated particle and V is the average velocity of the suspension in the streamwise direction. In the flow down an inclined plane, one has $V = 2/3V_s$ and v is the component of the settling velocity perpendicular to the plane, which yields

$$B = \frac{2}{3}\frac{\rho_p - \rho_l}{[\rho_p\beta_o + (1-\beta_o)\rho_l]\tan\theta} \tag{68}$$

Substituting the values of the current properties into (68) gives $B = 2.82$ with $h/a = 20$ and $\beta_o = 0.3851$. Curiously, these values lie really close to those used in the Stokesian Dynamics simulation by MB (see their table 1 and results of runs B and G1 with $\{B,h/a,\ \beta_o\} = \{3.4,30.54,0.4\}$ and $\{3.4,18.34,0.4\}$, respectively). It is found that the present drift-flux theory reproduces the heavy-over-light stratification reported in their simulations for a similar set of nondimensional parameters, though they studied a pressure driven flow. The nondimensional time t_{ss} elapsed to reach the steady-state in the Stokesian Dynamics simulations, obtained with $T = a/V$ as characteristic time, was of the order of $O(1600–4000)$. As commented above, see also Figure 5, the quasi-steady solution is reached in the present computation at $t_{ss} \approx 60/T = 3840$, in agreement with MB. Therefore, there is a great similarity between the present study and MB, where they proved for $h/a > 18$ that the suspension balance model predicts accurately similar flows. This fact shows nicely the value of the continuum approach and serves to understand the importance of accounting for particle migration, as for other free surface flows.[5]

Tip region of a falling suspension film: Homogeneous and resuspended regimes

In this section, the velocity and solid volumetric concentration profiles shown in Figure 4 are used as boundary conditions at the inlet of an open channel to study the advancing of thin suspension film down a constant slope bed. Recall that the plane is inclined at an angle of $\theta = 45°$. This example serves to clearly test the capability of the proposed theoretical/numerical formulation to cope with the advancing of a wetting front and migration of particles into the tip region.

To do so, an additional term was added to the RHS of the momentum balance equation (28) given in the spirit of Brackbill et al.[55] by $-\sigma\kappa\nabla\gamma$. Here σ is the coefficient of surface tension, $\kappa \equiv \nabla \cdot \vec{n}_{gl}$ is the local surface curvature, and $\vec{n}_{gl}$ is the unit normal vector to the interface drawn outwards from the gas to the liquid. The numerical treatment of such term is straightforward as is the same as for the buoyancy term $\vec{g}\cdot\vec{x}\nabla\rho$.

As starting point the homogeneous regime is simulated here by setting a fictitious slip velocity of $\vec{v}_r = 0$ for the same scenario described in the section entitled Viscous Resuspension in Uniform flow down an inclined plane, which results in the velocity profile shown in dashed line in Figure 4. The density and dynamic viscosity of the atmosphere are fixed much smaller than for the liquid, i.e. $\rho_g/\rho_l = \mu_g/\mu_l = 0.001$, and surface tension is set to $\sigma = 0.072$ kg s^{-2}. The computational domain is a structured mesh with $1000 \times 1 \times 100$ cells ($X \times Y \times Z$) and mesh size $\Delta X = \Delta Y = \Delta Z = 1.2 \times 10^{-4}$ m. Initial conditions are given by

$$\gamma = \beta = 0, \quad \vec{v} = \vec{u} = 0, \quad \hat{p} = 0 \tag{69}$$

As boundary conditions, periodic flow is imposed in the Y-direction for all the variables, inflow boundary condition at the inlet ($x = 0$), no slip at the bottom ($z = 0$), outflow condition at the outlet ($x = 0.12$ m) and atmospheric pressure and stress free condition at the top ($z = 0.012$ m)

$$\gamma = 1, \quad \beta = \beta_{\text{in}}(z), \quad \vec{v} = \vec{u} = U(z)\,\vec{e}_x, \quad (\nabla\hat{p})\cdot\vec{n} = 0 \quad \text{at } x = 0 \tag{70}$$

$$(\nabla\gamma)\cdot\vec{n} = (\nabla\beta)\cdot\vec{n} = 0, \quad \vec{v} = \vec{u} = 0, \quad (\nabla\hat{p})\cdot\vec{n} = 0 \quad \text{at } z = 0 \tag{71}$$

$$(\nabla\gamma)\cdot\vec{n} = (\nabla\beta)\cdot\vec{n} = 0, \quad (\nabla\vec{v})\cdot\vec{n} = (\nabla\vec{u})\cdot\vec{n} = 0, \quad (\nabla\hat{p})\cdot\vec{n} = 0 \quad \text{at } x = 0.12 \text{ m} \tag{72}$$

$$\gamma = \beta = 0, \quad (\nabla\vec{v})\cdot\vec{n} = (\nabla\vec{u})\cdot\vec{n} = 0, \quad \hat{p} = 0 \quad \text{at } z = 0.012 \text{ m} \tag{73}$$

where $\beta_{\text{in}}(z) = \beta_o$ and $U(z)$ is the Nusselt flat-film velocity profile in the homogeneous regime, shown in dashed line in Figure 4.

Figure 6a illustrates the propagation of the free surface interface down the inclined plane at several instants of time. At the very beginning, $t = 0.15$ s, very little fluid is injected at the bottom because of the vanishing streamwise velocity. Conversely, much more fluid comes into the computational domain close to $z = h$ because the velocity reaches its

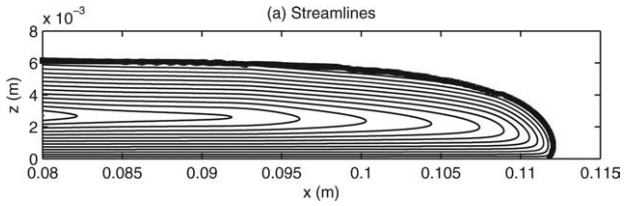

Figure 7. Detailed view of the streamlines associated with the relative velocity field $\vec{v} - (dx_f/dt)\vec{e}_x$ in the tip region as for Figure 6c.

Thin solid line marks up the free surface interface. (Aspect ratio 1:1)

maximum value there, see Figure 4a. As time proceeds the component of the gravitational force normal to the plane pulls the fluid downward and the tip region starts to develop. The flow close to the channel inlet becomes uniform and steady for larger time, $t > 2.9$ s, as shown by the free surface interface parallel to the plane. In the uniform region, the flow is, therefore, unidirectional and propagates parallel to the bottom bed. Moreover, the tip region is self-similar at those instants of time and the flow front propagates at a constant speed. Indeed, the velocity of the advancing front was computed by fitting the numerical values of the wetting front location $x_f(t)$, see Figure 6b, with a linear function of time, that yields $dx_f/dt = 0.020$ m s^{-1}. This value approaches well the theoretical value of 0.019 m s^{-1} obtained from conservation of mass by Hunt[56]

$$\frac{dx_f}{dt} = \frac{1}{h}\int_{z=0}^{z=h} \vec{v}(x=0,z)dz = \frac{\rho_p\beta_o + \rho_l(1-\beta_o)}{3\mu_m} g\, h^2\, \sin\theta \tag{74}$$

At this moment, it is important to point out the non-hydrostatic pressure distribution which is found out into the tip region. To this end, Figure 6c shows isolines of constant reduced pressure $\hat{p}$ at late time ($t = 5.4$ s), when the velocity of the wetting front tends to be constant. Interestingly, in the bulk of the flow, $x < 0.08$ m, such isolines are perpendicular to the inclined plane. This is a expected result because the free surface is parallel to the bed for $x < 0.08$ m, indicating that the velocity is parallel to the bottom. However, close to the wetting front, that is, for $0.08\ m < x < x_f$, the previous statement does not longer hold and a complex pressure distribution associated with the strong curvature of the free surface and velocities perpendicular to the bed is observed. A detailed view of the streamlines corresponding to the relative velocity field $\vec{v} - (dx_f/dt)\,\vec{e}_x$ close to the wetting front is shown in Figure 7, where the recirculation occurring in the tip region is readily depicted. Obviously, to solve with accuracy for the motion into the wetting front, the saddle-point problem described in the section entitled Finite volume discretization and solution procedure must be solved. As discussed below, solving accurately for the motion in the tip region is essential to compute correctly the dynamics of the flow in the resuspended regime.

Then the resuspended profile was simulated by activating the fluxes $\vec{v}_s$ (36), $\vec{v}_d$ (37), and $\vec{v}_{sh}$ (39) in the slip velocity. The computational extent was increased up to $z = 0.38$ m and the same type of initial and boundary conditions as described above was set. The unique difference with respect to the previous simulation is the velocity and concentration profiles at the inlet, which are the numerical solution computed in the section entitled Viscous resuspension in uniform flow down an inclined plane shown in continuous line in Figure 4. As for homogeneous flows, recall Figure 6a, the temporal evolution of the free surface is shown in Figure 8a. The first noticeable difference is the development of a front with higher depth than at the inflow. Indeed, the front depth increases as time proceeds from 6.25 mm ($t = 0$) to the asymptotic value of 8 mm (3.84 s). For $t > 3.84$ s the maximum depth at the tip region remains constant. Such increment in the maximum flow depth was not found in the homogoeneous regime (see Figure 6a). Next the location of the advancing front $x_f(t)$ is depicted in Figure 8b, and can be accurately fitted by a linear regression to yield the constant velocity of 0.02525 m s^{-1}. Therefore, the current streamwise extent is enough to ensure that the advancing front reaches a steady-state at late time.

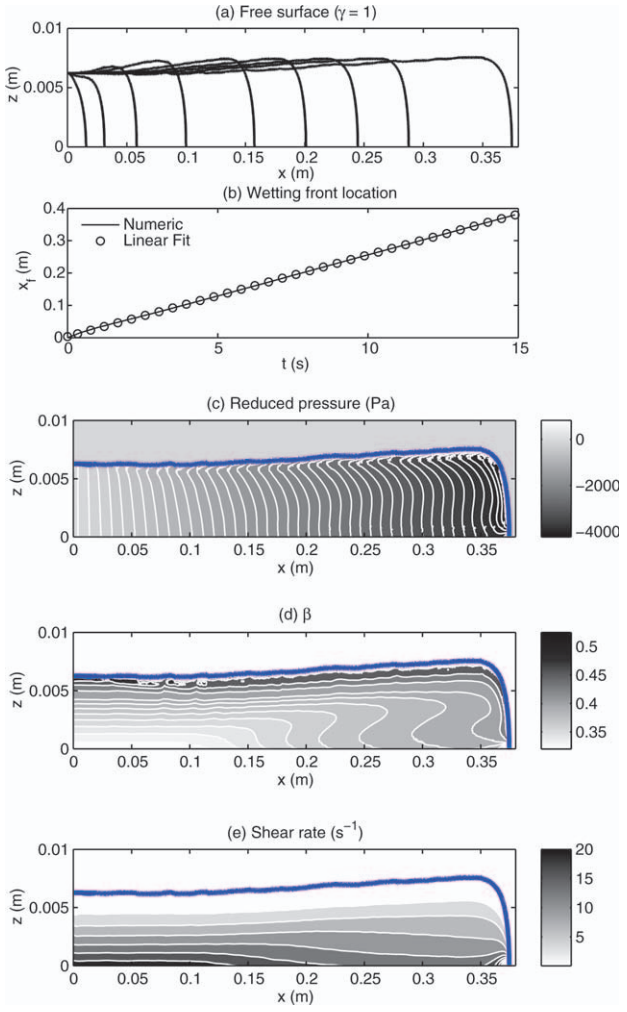

Figure 8. (a) Temporal evolution of the free surface interface for the resuspended inlet profiles in Figure 4 at t = 0.44, 1.00, 2.13, 3.84, 6.12, 7.83, 9.54, 11.25, and 14.67 s; (b) location of the wetting front as a function of time.

Isocontours of the reduced pressure $\hat{p}$ (c), solid volumetric concentration β (d), and shear rate (e) at $t = 14.67$ s. The thin solid line in (c)–(e) highlights the free surface. Aspect ratio in (a) and (c)–(e) is 10:1. [Color figure can be viewed in the online issue, which is available at wileyonlinelibrary.com.]

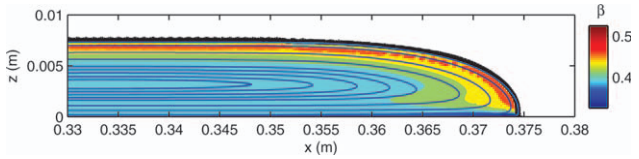

Figure 9. Detailed view of the streamlines associated with the relative velocity field $\vec{v} - (dx_f/dt)\vec{e}_x$ in the flow front as for Figures 8c–e.

Thin solid line marks up the free surface interface, while the color bar indicates the values of β. (Aspect ratio 1:1) [Color figure can be viewed in the online issue, which is available at wileyonlinelibrary.com.]

Indeed, at $t = 14.67$ s and behind the inlet ($x < 0.05$ m) the pressure distribution is nearly hydrostatic, the free-surface remains parallel to the bottom and solid particles move along the streamwise direction, as shown in Figures 8c–d. That is, the flow is uniform and steady, and is not affected by the tip region at $t = 14.67$ s and $x < 0.05$ m.

Therefore, it is interesting to analyze the flow field at $t = 14.67$ s and $x > 0.05$ m to better understand the dynamics of the dense suspension in the tip region. Downstream of $x = 0.05$ m, the isolines of reduced pressure deviate from the perpendicular to the bottom and their shapes are increasingly complex as approach the wetting front. Furthermore, this phenomenon is more pronounced in the present case than for the homogeneous regime, see Figure 6c, because the particle volumetric concentration is not longer constant in the resuspended regime. This fact is clearly understood taking into account that the streamwise velocity close to the free surface is maximum and decreases down to zero at the bottom bed. Moreover, the free surface velocity is larger than that of the advancing front. As a consequence, solid particles close to the free surface move faster than those located at lower depths and that the advancing front. So the upper solid particles try to recirculate as they reach the tip region, see Figure 9, increasing the solid volumetric concentration close to the inclined plane. However, the shear rate is higher at lower depths than at the free surface, see Figure 8e, and solid particles resuspend once again as they reach the bottom of the tip region because of the large values of the shear-induced self-diffusion velocity $\vec{v}_{sh}$. Indeed, the solid volumetric concentration depicted in Figure 9 illustrates this phenomenon and explains the accumulation of solid particles in the tip region, that is, the onset of the resuspended regime owing the increment of flow depth observed in Figure 8a. Obviously, at late time ($t = 14.67$ s) the solid particle dynamics in the tip region affects the bulk of the flow, $0.1 < x < 0.35$ m, where the flow depth monotonously increases in the downstream direction, see Figures 8c–e. For instance, the effect of the recirculation of solid particles is apparent on the curved lines of constant β depicted in Figure 8d. Such complex profiles of the solid concentration are one of the causes of the complex pressure distribution shown in Figure 8c, which is really difficult to prescribe *a priori*.

It is worth mentioning that the aspect ratio of the vertical to the horizontal length scales, that is, the shallowness parameter ε, varies during the flow from $\varepsilon \to \infty$ ($t = 0$) to $\varepsilon \approx 1/50$ ($t \approx 15$ s). The actual formulation is valid for arbitrary values of ε and is able to solve with success for viscous shallow particle-laden flows with $\varepsilon \ll 1$. Indeed, the shallowness parameter ε could be decrease as necessary by increasing the length of the computational domain because the physical formulation described in the section entitled Formulation of the Problem does not impose any restriction on it. Furthermore, the current formulation is valid for arbitrary bottom slopes because it avoids assumptions on the mixture pressure distribution, which is solved locally at every time step.

Roll waves in viscous flow

Yih[57] and Liu et al.,[58] among others, studied the stability of a uniform viscous flow down an inclined plane. They showed that free surface instabilities develop for Reynolds numbers, Re, larger than a threshold Re_c, where

$$\mathrm{Re} = \frac{g\,\rho_l^2\,\sin\theta\,h^3}{3\mu_l^2} \tag{75}$$

and $\mathrm{Re}_c = 5/6$ cotan θ[57] or $\mathrm{Re}_c = 5/4$ cotan θ.[58] As in previous sections, θ denotes the angle of the plane with respect to the horizontal and h is the Nusselt flat-film thickness. Figure 10 depicts the critical Reynolds number as a function of θ. Notice that Re_c decreases suddenly with θ, taking values lower than 10 for $\theta > 7°$.

Therefore, it is natural to find free surface instabilities, hereafter referred to as *viscous roll waves*, in thin film flows down inclined and vertical planes, see for instance Usha et al.,[2] Kalliadasis et al.,[3] Malamataris and Balakotaiah,[12] and Mudunuri and Balakotaiah.[59] Here the capabilities of the implemented numerical scheme to compute viscous roll waves are illustrated by reproducing previous experiments and hydrodynamic stability analysis by Tihon et al.[60] and Plaschko and Schaflinger[61] for one- and two-layer thin film flows, respectively.

Tihon et al.[60] characterized the temporal frequency f of solitary waves at the Reynolds numbers of 14, 35, and 57 for a plane inclined at an angle of $\theta = 5°$, see Figure 11a. To compare the numerical frequency with their experimental results for a given wavelength λ, the nondimensional frequency and wavelength are represented in logarithmic scale in Figure 11b. Without loss of generality, λ and f were made dimensionless using the quantities h and $\rho_l h^2/\mu_l$ as length and temporal scales, respectively. So the nondimensional wavelength $\hat{\lambda} \equiv \lambda/h$ and the nondimensional frequency $\hat{f} \equiv f\rho_l h^2/\mu_l$ were defined. The first interesting finding is the linear dependence of $\log(\hat{\lambda})$ and $\log(\hat{f})$ at all Reynolds numbers. This fact allows the extrapolation of experimental results from long wavelengths ($\hat{\lambda} > 100$) to shorter wavelengths ($\hat{\lambda} < 100$). Three wavelengths ($\hat{\lambda} = 40$, 80, and 120) were simulated for the Reynolds number of Re = 14 and the Bond number of $\mathrm{Bo} \equiv \rho_l g h^2/\sigma = 0.25$. The density and dynamic viscosity of the atmosphere are set much smaller

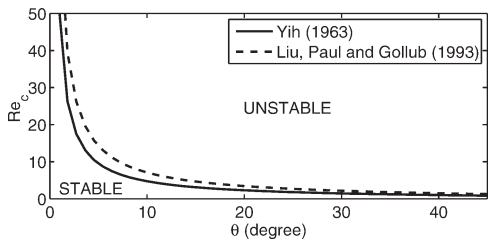

Figure 10. Critical Reynolds number for the inception of roll waves in a viscous uniform flow.

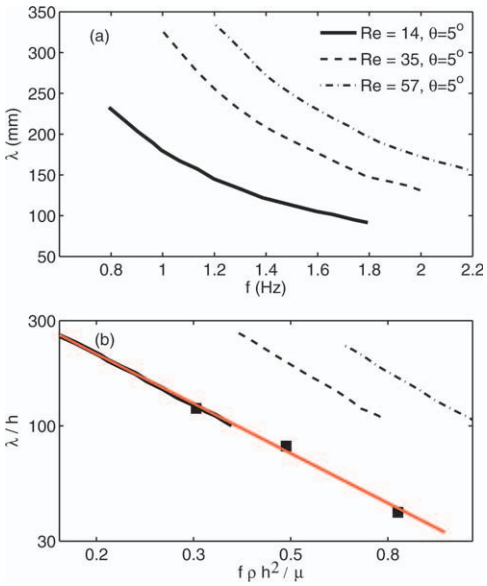

Figure 11. Spatial wavelength λ vs. temporal frequency f in the experiments by Tihon et al.:[60] dimensional values in linear scale (a) and nondimensional values in logarithmic scale (b).

Also, in panel (b) it is shown with solid squares and red solid line, respectively, the numerical results and the linear fit of experiments at Re = 14. [Color figure can be viewed in the online issue, which is available at wileyonlinelibrary.com.]

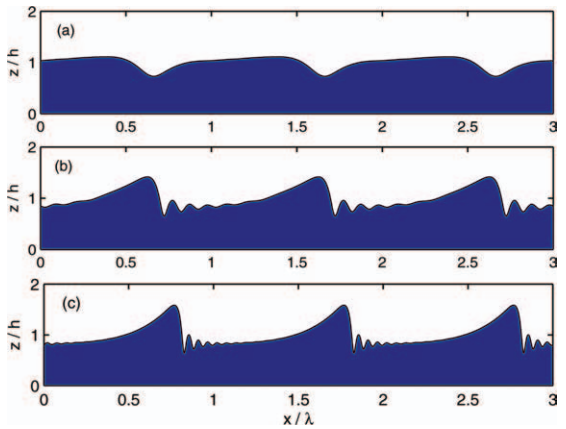

Figure 12. Flow depth for roll waves with base flow parameters of Re = 14 and θ = 5°: (a) λ/h = 40, (b) λ/h = 80, and, (c) λ/h = 120.

The temporal frequency of the non-linear limit cycle is shown with filled squares in Figure 11b and agrees with previous experimental results. [Color figure can be viewed in the online issue, which is available at wileyonlinelibrary.com.]

than for the liquid, $\rho_g/\rho_l = \mu_g/\mu_l = 0.001$. The computational domain is a structured mesh with $2700 \times 1 \times 90$ cells ($X \times Y \times Z$) and nondimenional lengths of $0 \leq x/h \leq 3\hat{\lambda}$, $0 \leq y/h \leq 0.02$ and $0 \leq z/h \leq 2$. Initial conditions are given by

$$\gamma = \begin{cases} 1 & \text{if } 0 \leq z/h \leq 1 + \delta \sin(2\pi x/h/\hat{\lambda}), \\ 0 & \text{if } 1 + \delta \sin(2\pi x/h/\hat{\lambda}) < z/h \leq 2, \end{cases}$$
$$\beta = 0, \quad \vec{v} = \vec{u} = 0, \quad \hat{p} = 0 \quad (76)$$

As boundary conditions no slip is imposed at the bottom ($z = 0$), atmospheric pressure ($p = p_a$) and stress free condition at the top ($z/h = 2$) and periodic flow at $x = 0$, $x/h = 3\ \hat{\lambda}$ and along the Y-direction. In Eq. 76, $\delta = 0.5$ corresponds with the amplitude of a sinusoidal perturbation, though lower values could also be used.

Periodic limit cycles at late time were found in the three cases, corresponding with monochromatic waves. Figure 12 illustrates the shapes of the final roll waves, when the flows reached the saturated periodic regime. The ensuing temporal frequency agrees very well with previous known results, see Figure 11b. The aspect of the roll wave depends on the spatial wavelength or temporal frequency: as the wavelength increases, the depth of the bore grows. Indeed, the flow becomes very steep for $\hat{\lambda} \geq 80$ and, subsequently, short-wavelength secondary instabilities develop in front of the solitary bore. Secondary waves reflect the effect of surface tension and vertical acceleration.[60,62] Furthermore, the well-known result that the pressure is hydrostatic everywhere except in front of the solitary hump, where secondary instabilities occur,[62] is corroborated in Figure 13a. Secondary instabilities modify drastically the local flow field in front of the solitary bore, induce a marked up depression that cannot be explained by means of hydrostatic models and significantly increase the shear stress between the film and the wall,[60,62] as shown in Figure 13b.

To the best of the author's knowledge, previous studies analyzing the influence of solid particle migration on the stability of dense suspension films are scarce. Solid particles may play an important role on the free surface instability because of their effects on the flat-film base state and the perturbed flow. On the one hand, in the homogeneous case, the background flow remains unaltered and, therefore, one would expect a negligible influence of solid particles on the stability criteria,[57,58] though the final nonlinear saturated state may change due to the non-uniform shear-rate field. On the other hand, the problem for settled and risen suspensions

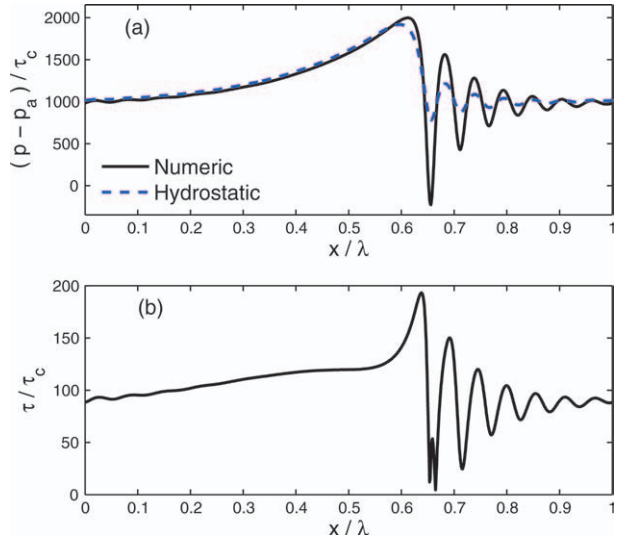

Figure 13. Nondimensional pressure (a) and shear stress (b) at the bottom for the roll wave in Figure 12c, with $\tau_c = \mu_l^2/(\rho_l h^2)$.

[Color figure can be viewed in the online issue, which is available at wileyonlinelibrary.com.]

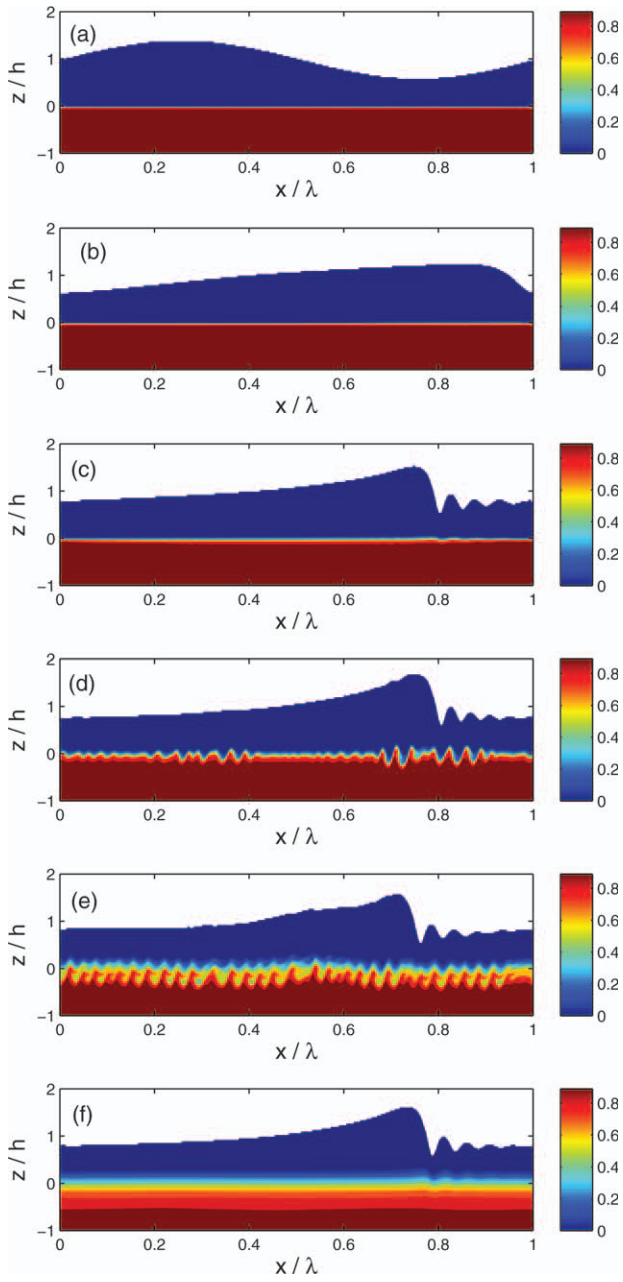

Figure 14. Sequence of snapshots illustrating the temporal evolution of the solid volumetric concentration β/β_M in the liquid phase.

[Color figure can be viewed in the online issue, which is available at wileyonlinelibrary.com.]

is more complicated because the ensuing base state exhibits density gradient. In the case of viscous resuspended suspensions, Carpen and Brady[63] suggested that heavy-over-light stratification might be unstable to spanwise perturbations, similar to rapid granular flows, owing the formation of longitudinal vortices that may also be unstable to longitudinal disturbances.[61] In the settled regime, a clear liquid layer appears above the settled suspension, leading to two-layer gravity driven film flow with free surface. Plaschko and Schaflinger[61] investigated the stability of this flow supposing a constant concentration of solid particles below a clear liquid and found the existence of two different instabilities (waves at the free surface and interfacial waves) which are described next.

The computational domain was enlarged along the z-axis up to the range of $-1 \leq z/h \leq 2$, while the streamwise length was decreased down to $0 \leq x/h \leq \hat{\lambda}$, maintaining the same mesh size as in the previous simulation. Initial conditions are now given by

$$\gamma = \begin{cases} 1 & \text{if } -1 \leq z/h \leq 1 + \delta \sin(2\pi x/h/\hat{\lambda}), \\ 0 & \text{if } 1 + \delta \sin(2\pi x/h/\hat{\lambda}) < z/h \leq 2, \end{cases}$$

$$\beta = \begin{cases} \beta_o & \text{if } -1 \leq z/h \leq 0, \\ 0 & \text{if } 0 < z/h \leq 2, \end{cases} \qquad \vec{v} = \vec{u} = 0, \quad \hat{p} = 0, \qquad (77)$$

with $\beta_o = 0.9\ \beta_M$, see Figure 14a. Finally, the same set of boundary conditions were imposed with $\rho_p/\rho_l = 1$, Re $= 14$ and $\hat{\lambda} = 120$. The slip velocity was neglected[61] ($\vec{v}_r = 0$).

Figure 14 shows some snapshots at six instants of time of the field $\beta(x,z)$ normalized with β_M, illustrating the initial condition of the volumetric concentration (panel a), the formation of the main surge (panel b), the development of secondary instabilities close to the solitary hump (panel c) that excite interfacial waves amplifying downstream (panel d), and the wave breaking process (panel e) that originates a detached layer of particles moving above the original interface (panel f). During the formation of the main bore, see Figure 14b, and the growth of secondary instabilities in its front, see Figure 14c, there is no interfacial instability. So the surge develops in the upper layer analogous to the case in the absence of solid particles, see Figure 12c, due to the high viscosity of the lower layer. However, when secondary instabilities are fully developed, non-uniform pressure (Figure 13a) and shear stress (Figure 13b) oscillations excite unstable interfacial modes, see Figure 14d, originating interfacial waves with wavelengths much shorter than the roll wave length $\hat{\lambda}$. Indeed, by inspecting Figure 14d, it is found that bed forms wavelengths are the same as that of the secondary instabilities in front of the solitary wave. This fact highlights the relevance of including surface tension, the real pressure, and the vertical velocity component in the actual model, which are responsible for the formation of secondary waves. Interfacial waves grow as they are convected along the streamwise direction, see Figure 14e, but move slower than roll waves because of their higher viscosity. Consequently, pressure and shear stress oscillations persist on the sediment interface, interact with the bed forms and accelerate the wave breaking, owing the mix of the dense suspension and the clear liquid layer at late time. Hence, the original sharp interface between layers is destroyed and a multilayer configuration develops in the bed, as shown in Figure 14f, owing a periodic state. This phenomenology is in agreement with Plaschko and Schaflinger[61] stability results.

Conclusions

A numerical formulation for falling liquid films carrying monodisperse spheres under the action of gravity in Newtonian regime has been proposed. By adopting the algebraic drift-flux model for the slip velocity $\vec{v}_r$, see Eqs. 34–39, the theoretical model and the finite volume method have been verified with several examples to analyze high viscous flows in the presence of sharp discontinuities of the volumetric concentrations β and γ, namely that: vertical settlers, falling suspension films, and viscous roll waves.

Some advantages of the proposed formulation are the following: it works with success for arbitrary values of the flow

depth, solid volumetric concentration, and bed slope; the advancing of the wetting front down an inclined plane can be analyzed properly; the formulation is neither based on depth-averaging nor on a hydrostatic pressure assumption and, hence, is valid for arbitrary values of the shallowness parameter; the proposed model is valid for homogeneous and resuspended suspensions; viscous roll waves can be computed with success, accounting for the non-hydrostatic pressure distribution, the complete velocity field and surface tension effects for a wide range of spatial wavelengths.

From the author's point of view, in addition to reduced order models such as boundary-layer, averaged models and single surface equations, see Usha et al.[2] and Kalliadasis et al.,[3] as well as more complex mesoscopic and microscopic models, see Fox,[6] the Navier–Stokes model proposed here may contribute to better understand falling suspension films as well as free surface flows carrying monodisperse spheres in other contexts.

Acknowledgment

This work has been supported by the Spanish MINECO (project # DPI2011-28356-C03-03), Junta de Andalucía (project # TEP-07495), EU funds and the research stay grant at the University of Southampton from the Universidad de Jaén. The computer time was provided by Centro Informático Científico de Andalucía, ECIENCIA-CICA.

Literature Cited

1. Chang C, Powell RL. Hydrodynamic transport properties of concentrated suspensions. *AIChE J*. 2002;48:2475–2480.
2. Usha R, Sharma A, Dandapat BS. Wave Dynamics and Stability of Thin Film Flow Systems. *Chenai: Narosa*, 2006.
3. Kalliadasis S, Ruyer-Quil C, Scheid B, Velarde MG. *Falling Liquid Films*. London: Springer, 2012.
4. Timberlake BD, Morris JF. Particle migration and free-surface topography in inclined plane flow of a suspension. *J Fluid Mech*. 2005;538:309–341.
5. Min KH, Kim C. Simulation of particle migration in free-surface flows. *AIChE J*. 2010;56:2539–2550.
6. Fox RO. Large-eddy-simulation tools for multiphase flows. *Annu Rev Fluid Mech*. 2011;44:47–76.
7. Gopala VR, van Wachem BGM. Volume of fluid methods for immiscible-fluid and free-surface flows. *Chem Eng J*. 2008;141:204–221.
8. Passalacqua A, Fox RO. Implementation of an iterative solution procedure for multi-fluid gas-particle flow models on unstructured grids. *Powder Technol*. 2011;213:174–187.
9. Van Wachem BGM, Schouten JC, van den Bleek CM, Krishna R, Sinclair JL. Comparative analysis of CFD models of dense gas-solid systems. *AIChE J*. 2001;47:1035–1051.
10. Van Wachem BGM, Almstedt AE. Methods for multiphase computational fluid dynamics. *Chem Eng J*. 2003;96:81–98.
11. Hiltunen K, Jäsberg A, Kallio S, Karema H, Kataja M, Koponen A, Manninen M, Taivassalo V. *Multiphase Flow Dynamics. Theory and Numerics. Tech. Rep. 722*, VTT Publications. 2009.
12. Malamataris NA, Balakotaiah V. Flow structure underneath the large amplitude waves of a vertically falling film. *AIChE J*. 2008;54:1725–1740.
13. Unverdi SO, Tryggvason G. A front-tracking method for viscous, incompressible, multi-fluid flows. *J Comput Phys*. 1992;100:25–37.
14. Ishii M, Hibiki T. *Thermo-Fluid Dynamics of Two-Phase Flow*. 2nd ed. New York: Springer, 2011.
15. LeVeque RJ. High-resolution conservative algorithms for advection in incompressible flow. *SIAM J Numer Anal*. 1996;33:627–665.
16. Jenkins JT, Savage SB. Theory for the rapid flow of identical, smooth, nearly elastic, spherical particles. *J Fluid Mech*. 1983;130:187–202.
17. Campbell CS. Rapid granular flows. *Annu Rev Fluid Mech*. 1990;22:57–92.
18. Gidaspow D. *Multiphase Flow and Fluidizationx: Continuum and Kinetic Theory Descriptions*. San Diego: Academic Press, 1994.
19. Goldhirsch I. Rapid granular flows. *Annu Rev Fluid Mech*. 2003;35:267–293.
20. Stickel JJ, Powell RL. Fluid mechanics and rheology of dense suspensions. *Annu Rev Fluid Mech*. 2005;37:129–149.
21. Sethian JA, Smereka P. Level set methods for fluid interfaces. *Annu Rev Fluid Mech*. 2003;35:341–372.
22. Ferziger JH. Interfacial transfer in Tryggvason's method. *Int J Numer Meth Fluids*. 2003;41:551–560.
23. Nir A, Acrivos A. Sedimentation and sediment flow on inclined surfaces. *J Fluid Mech*. 1990;212:139–153.
24. Schaflinger U, Acrivos A, Zhang K. Viscous resuspension of a sediment within a laminar and stratified flow. *Int J Multiphase Flow*. 1990;16:567–578.
25. Schaflinger U, Acrivos A, Stivi H. An experimental-study of viscous resuspension in a pressure-driven plane channel flow. *Int J Multiphase Flow*. 1995;21:693–704.
26. Kapoor B, Acrivos A. Sedimentation and sediment flow in settling tanks with inclined walls. *J Fluid Mech*. 1995;290:39–66.
27. Leighton D, Acrivos A. The shear-induced migration of particles in concentrated suspensions. *J Fluid Mech*. 1987;181:415–439.
28. Leighton D, Acrivos A. Viscous resuspension. *Chem Eng Sci*. 1986;41:1377–1384.
29. Zhang K, Acrivos A. Viscous resuspension in fully-developed laminar pipe flows. *Int J Multiphase Flow*. 1994;20:579–591.
30. Nott PR, Brady JF. Pressure-driven flow of suspensions: simulation and theory. *J Fluid Mech*. 1994;275:157–199.
31. Richardson JF, Zaki WN. Sedimentation and fluidisation: Part 1. *Trans Instm Chem Engrs*. 1954;32:35–53.
32. Morris JF, Brady JF. Pressure-driven flow of a suspension: buoyancy effects. *Int J Multiphase Flow*. 1998;24:105–130.
33. Morris JF, Boulay F. Curvilinear flows of noncolloidal suspensions: the role of normal stresses. *J Rheol*. 1999;43:1213–1237.
34. Patankar SV. *Numerical Heat Transfer and Fluid Flow. Series in Computational Methods in Mechanics and Thermal Sciences*. Washington: Taylor & Francis, 1980.
35. Ferziger JH, Perić M. *Computational Methods for Fluid Dynamics*. 3rd ed. Berlin: Springer, 2002.
36. Ungarish M. *Hydrodynamics of Suspensions: Fundamentals of Centrigugal and Gravity Separation*. Berlin: Springer-Verlag, 1993.
37. Rhie CM, Chow WL. Numerical study of the turbulent flow past an airfoil with trailing edge separation. *AIAA J*. 1983;21:1525–1532.
38. Jasak H. Error analysis and estimation in the finite volume method with applications to fluid flows. Ph.D. thesis, Imperial College, University of London, 1996.
39. Rusche H. Computational fluid dynamics of dispersed two-phase flows at high phase fractions. Ph.D. thesis, Imperial College, University of London, 2002.
40. Zalesak T. Fully multidimensional flux-corrected transport algorithms for fluids. *J Comput Phys*. 1979;31:335–362.
41. Bohorquez P. Competition between kinematic and dynamic waves in floods on steep slopes. *J Fluid Mech*. 2010;645:375–409.
42. Muzaferija S, Perić M. *Computation of free surface flows using interface-tracking and interface-capturing methods*. In: Mahrenholtz O, Markiewicz, editors. *Nonlinear Water Waves Interaction*. Southampton: WIT Press, 1998: Chap. 2, 59–100.
43. Berberović E, Van Hinsberg NP, Jakirlić S, Roisman IV, Tropea C. Drop impact onto a liquid layer of finite thickness: dynamics of the cavity evolution. *Phys Rev E*. 2009;79:036306.
44. Jasak H, Weller HG, Gosman AD. High resolution NVD differencing scheme for arbitrarily unstructured meshes. *Int J Numer Meth Fluids*. 1999;31:431–449.
45. Deshpande SS, Trujillo MF, Wu X, Chahine G. Computational and experimental characterization of a liquid jet plunging into a quiescent pool at shallow inclination. *Int J Heat Mass Trans*. 2012;34:1–14.
46. OpenCFD. *OpenFOAM—The Open Source CFD Toolbox—User's Guide*, 1st ed. United Kingdom: OpenCFD Ltd., 2010.
47. OpenCFD. *OpenFOAM—The Open Source CFD Toolbox—Programmer's Guide*, 1st ed, United Kingdom: OpenCFD Ltd., 2010.
48. Snabre P, Pouligny B, Metayer C, Nadal F. Size segregation and particle velocity fluctuations in settling concentrated suspensions. *Rheol Acta*. 2009;48:855–870.
49. Mills P, Snabre P. Settling of a suspension of hard spheres. *Europhys Lett*. 1994;25:651–656.
50. Sweby PK. High resolution schemes using flux limiters for hyperbolic conservation laws. *SIAM J Numer Anal*. 1984;21:995–1011.
51. Phillips RJ, Brady JF, Bossis G. A constitutive equation for concentrated suspensions that accounts for shear-induced particle migration. *Phys Fluids*. 1992;4:30–40.
52. Cook BP. Theory for particle settling and shear-induced migration in thin-film liquid flow. *Phys Rev E*. 2008;78:045303.
53. Andreini N. Dam break of Newtonian fluids and granular suspensions: internal dynamics measurements. Ph.D. thesis, Ecole Polytechnique Fédérale de Lausanne, 2012.

54. Barenblatt GI. *Scaling, Self-Similarity, and Intermediate Asymptotics*. Cambridge: Cambridge University Press, 1996.
55. Brackbill JU, Kothe DB, Zemach C. A continuum method for modeling surface-tension. *J Comput Phys*. 1992;100:335–354.
56. Hunt B. Newtonian fluid mechanics treatment of debris flows and avalanches. *J Hydraul Eng*. 1994;120:1350–1363.
57. Yih CS. Stability of liquid flow down an inclined plane. *Phys Fluids*. 1963;6:321–334.
58. Liu J, Paul JD, Gollub JP. Measurements of the primary instabilities of film flows. *J Fluid Mech*. 1993;250:69–101.
59. Mudunuri RR, Balakotaiah V. Solitary waves on thin falling films in the very low forcing frequency limit. *AIChE J*. 2006;52:3995–4003.
60. Tihon J, Serifi K, Argyriadi K, Bontozoglou V. Solitary waves on inclined films: their characteristics and the effects on wall shear stress. *Exp Fluids*. 2006;41:79–89.
61. Plaschko P, Schaflinger U. Absolute instabilities in two-layer gravity driven film flow with a free surface. *Z Angew Math Phys*. 1998;49:194–204.
62. Malamataris NA, Vlachogiannis M, Bontozogloua V. Solitary waves on inclined films: Flow structure and binary interactions. *Phys Fluids*. 2002;14:1082–1094.
63. Carpen IC, Brady JF. Gravitational instability in suspension flow. *J Fluid Mech*. 2002;472:201–210.

Appendix A. Full Eulerian Model

To derive an additional partial differential equation for $\vec{v}_r$ that accounts for the relative inertia of the solid particles with respect to the liquid, one can apply the change rule to the LHS of (18)–(19) and, taking into account (1)–(2), yields

$$\frac{\partial \vec{v}_l}{\partial t} + (\vec{v}_l \cdot \nabla)\vec{v}_l = \frac{1}{\alpha_l \rho_l}\left[\alpha_l \rho_l \vec{g} - (1-\alpha_p)\nabla p_l - K(\vec{v}_l - \vec{v}_p) + \nabla \cdot (\alpha_l \bar{\bar{\tau}}_l')\right] \quad \text{(A1)}$$

$$\frac{\partial \vec{v}_p}{\partial t} + (\vec{v}_p \cdot \nabla)\vec{v}_p = \frac{1}{\alpha_p \rho_p}\left[\alpha_p \rho_p \vec{g} - \alpha_p \nabla p_l + K(\vec{v}_l - \vec{v}_p) - \nabla p_p + \nabla \cdot (\alpha_p \bar{\bar{\tau}}_p')\right] \quad \text{(A2)}$$

From (21), (31), and (33) the particle stress tensor in the suspension is given by

$$\alpha_p \bar{\bar{\tau}}_p' = 2\mu_m \bar{\bar{\gamma}} - \alpha_l \bar{\bar{\tau}}_l' \quad \text{(A3)}$$

Then, Eqs. A1–A3 can be simplified by recalling that inside the dense suspension $\gamma = 1$, that is, $\alpha_l = 1 - \alpha_p$ with $\alpha_p = \beta$, and $p_l = p - p_p$ (29). Also, by definition (11), it is known that $\vec{v}_p = \vec{v}_l + \vec{v}_r$. Substituting this relation into (A2), and taking into account (A1)–(A3), one has

$$\frac{\partial \vec{v}_r}{\partial t} + \nabla \cdot (\vec{v}\vec{v}_r) + \nabla \cdot [w\vec{v}_r\vec{v}_r] - [\nabla \cdot (\vec{v} + 2\vec{v}_r)]\vec{v}_r + K\left(\frac{1}{\beta\rho_p} + \frac{1}{(1-\beta)\rho_l}\right)\vec{v}_r = \frac{\rho_p - \rho_l}{\rho_p \rho_l}\nabla p - \left(\frac{1}{\beta\rho_p} - \frac{1}{\rho_p} + \frac{1}{\rho_l}\right)\nabla p_p + \frac{1}{\beta\rho_p}\nabla \cdot \left(2\mu_m \bar{\bar{\gamma}}\right) - \left[\frac{1}{(1-\beta)\rho_l} + \frac{1}{\beta\rho_p}\right]\nabla \cdot [(1-\beta)\bar{\bar{\tau}}_l'] \quad \text{(A4)}$$

where $w \equiv 2 - \beta(1+s)/(1+\beta s)$. Given a known solid volumetric concentration β, pressure p and velocity field $\vec{v}$ of the mixture, one can solve implicitly (A4) to obtain $\vec{v}_r$.

Manuscript received Mar. 16, 2012, and revision received May 16, 2012.